

## Article

# Molecular Docking, DFT Calculations, Effect of High Energetic Ionizing Radiation, and Biological Evaluation of Some Novel Metal (II) Heteroleptic Complexes Bearing the Thiosemicarbazone Ligand

Ehab M. Abdalla <sup>1</sup> , Safaa S. Hassan <sup>2</sup>, Hussein H. Elganzory <sup>3,\*</sup> , Samar A. Aly <sup>4</sup> and Heba Alshater <sup>5</sup>

<sup>1</sup> Chemistry Department, Faculty of Science, New Valley University, Alkharga 72511, Egypt; ehababdalla99@sci.nvu.edu.eg

<sup>2</sup> Chemistry Department, Faculty of Science, Cairo University, Giza 12613, Egypt; hsafaa@sci.cu.edu.eg

<sup>3</sup> Department of Chemistry, College of Science, Qassim University, Buraidah 51452, Saudi Arabia

<sup>4</sup> Department of Environmental Biotechnology, Genetic Engineering and Biotechnology Research Institute, University of Sadat City, Sadat City 32958, Egypt; samar.mostafa@gabri.usc.edu.eg

<sup>5</sup> Department of Forensic Medicine and Clinical Toxicology, University Hospital, Menoufia University, Shebin El-Kom 32511, Egypt; heba.alshater@med.menofia.edu.eg

\* Correspondence: hhsien@qu.edu.sa; Tel.: +966-56-810-9592



**Citation:** Abdalla, E.M.; Hassan, S.S.; Elganzory, H.H.; Aly, S.A.; Alshater, H. Molecular Docking, DFT Calculations, Effect of High Energetic Ionizing Radiation, and Biological Evaluation of Some Novel Metal (II) Heteroleptic Complexes Bearing the Thiosemicarbazone Ligand. *Molecules* **2021**, *26*, 5851. <https://doi.org/10.3390/molecules26195851>

Academic Editor: Susana Ibáñez Maella

Received: 8 August 2021

Accepted: 23 September 2021

Published: 27 September 2021

**Publisher's Note:** MDPI stays neutral with regard to jurisdictional claims in published maps and institutional affiliations.



**Copyright:** © 2021 by the authors. Licensee MDPI, Basel, Switzerland. This article is an open access article distributed under the terms and conditions of the Creative Commons Attribution (CC BY) license (<https://creativecommons.org/licenses/by/4.0/>).

**Abstract:** New Pb(II), Mn(II), Hg(II), and Zn(II) complexes, derived from 4-(4-chlorophenyl)-1-(2-(phenylamino)acetyl)thiosemicarbazone, were synthesized. The compounds with general formulas,  $[Pb(H_2L)_2(OAc)_2] \cdot ETOH \cdot H_2O$ ,  $[Mn(H_2L)(HL)]Cl$ ,  $[Hg_2(H_2L)(OH)SO_4]$ , and  $[Zn(H_2L)(HL)]Cl$ , were characterized by physicochemical and theoretical studies. X-ray diffraction studies showed a decrease in the crystalline size of compounds that were exposed to gamma irradiation ( $\gamma$ -irradiation). Thermal studies of the synthesized complexes showed thermal stability of the Mn(II) and Pb(II) complexes after  $\gamma$ -irradiation compared to those before  $\gamma$ -irradiation, while no changes in the Zn(II) and Hg(II) complexes were observed. The optimized geometric structures of the ligand and metal complexes are discussed regarding density functional theory calculations (DFT). The antimicrobial activities of the ligand and metal complexes against several bacterial and fungal stains were screened before and after irradiation. The Hg(II) complex has shown excellent antibacterial activity before and after  $\gamma$ -irradiation. In vitro cytotoxicity screening of the ligand and the Mn(II) and Zn(II) complexes before and after  $\gamma$ -irradiation disclosed that both the ligand and Mn(II) complex exhibited higher activity against human liver (Hep-G2) than Zn(II). Molecular docking was performed on the active site of MK-2 and showed good results.

**Keywords:** DFT calculations;  $\gamma$ -irradiation; anticancer; complexes; docking; thiosemicarbazone

## 1. Introduction

Thiosemicarbazones (TSCs) are a class of inorganic metal chelators that exhibit various complexes with transition metals, including Cu, Pd, Ni, and others [1,2]. TSCs and their metal complexes have interesting chemistry because of their variable bonding modes, promising biological implications, structural diversity, and ion-sensing ability [3]. In addition, they have been used as drugs and possess a wide range of biological activities, such as antibacterial [4], antifungal [5,6], antiviral [7], antiamebic [8], antimalarial [9], and antitumor [10] effectiveness. Numerous literature studies have presented that the biological properties of metal complexes with NS, ONS, and ONN chelating thiosemicarbazones derivatives using various carbonyl compounds, and its complexes [11], are analogs to the metallo-salen compounds of the O,N,N,O-chelating set and have biologically active structures. Antimicrobial activity of vanillin-4-methyl-4-phenyl-3-thiosemicarbazone complexes with cobalt(II), nickel(II), copper(II), and zinc(II) metal ions were examined against

Gram-positive, Gram-negative bacteria, and two fungal pathogens. Copper and zinc complexes of vanillin thiosemicarbazone have higher antibacterial and antifungal activities than other complexes [12]. Previous studies manifested the impact of  $\gamma$ -irradiation on the thermal decomposition, spectral, X-ray diffraction, and surface morphology of complexes of transition metals [13]. Furthermore,  $\gamma$ -radiation can influence the color, chemical composition, and catalytic properties, as well as the magnetic, structural, optical, electrical, thermal, and biological activities of sorts of solids [14]. The crystallinity, surface area, particle size, and position and intensity of the characteristic bands in FT-IR and electronic spectral studies of solid materials were shown to be altered [15,16]. Several studies showed the alteration in the antibacterial activity of different tested materials upon exposure to  $\gamma$ -irradiation [17]. Here, we report the synthesis and characterization of complexes of Pb(II), Mn(II), Hg(II), and Zn(II) with the ligand 4-(4-chlorophenyl)-1-(2-(phenylamino)acetyl)thiosemicarbazone. The aim of this work is to study the effect of  $\gamma$ -irradiation on the ligand and its complexes. The FT-IR, UV-Vis absorption spectra, TG/DTG, and X-ray diffraction patterns were studied. The antibacterial, antifungal, and anti-cancer activities of the ligand and its metal complexes before and after  $\gamma$ -irradiation were evaluated.

## 2. Experimental

### 2.1. Material and Methods

All organic compounds and solvents were purchased from Fluka or Merck, Naser City, Egypt. The metal salts  $\text{Pb}(\text{CH}_3\text{COO})_2$ ,  $\text{MnCl}_2$ ,  $\text{HgSO}_4$ , and  $\text{ZnCl}_2$  were obtained from Fluka and then used for complex synthesis without further purification.

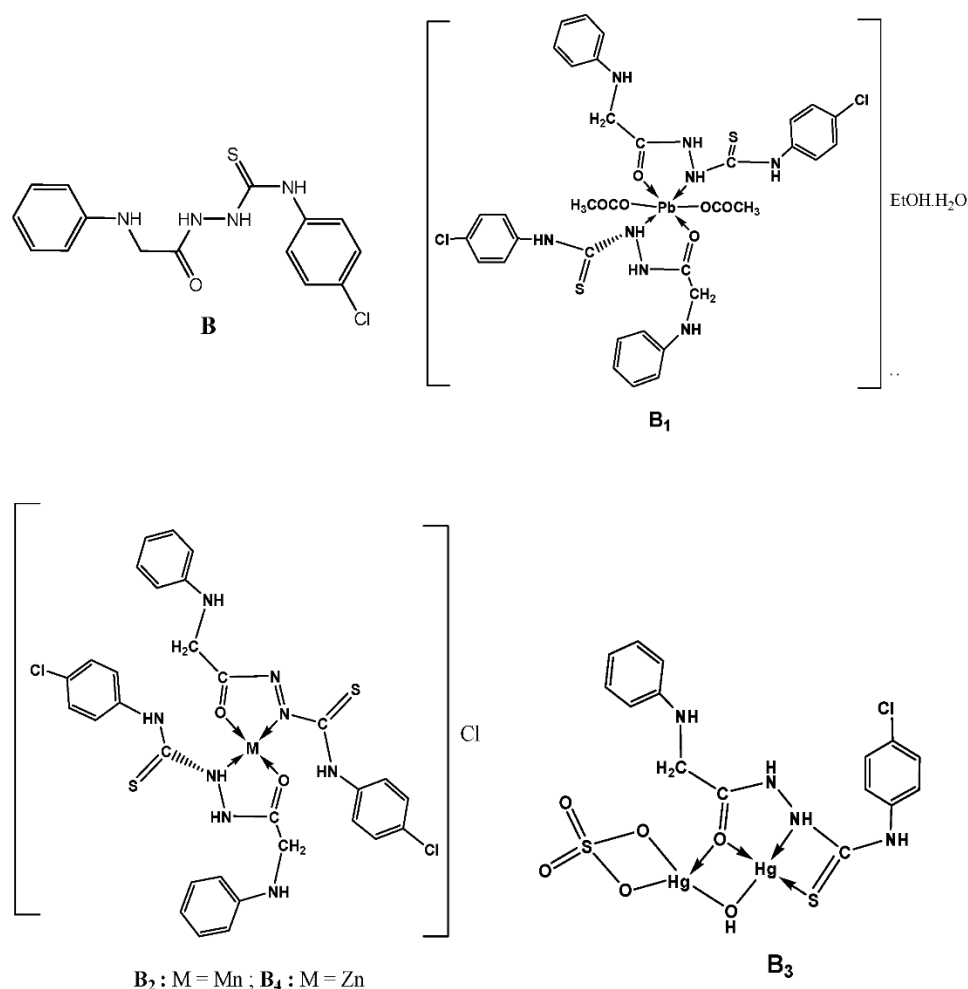
### 2.2. Synthesis of Metal Complexes

Different metal complexes were synthesized by stoichiometric addition of an ethanolic solution of metal salts ( $\text{MX}_2$ ) (where  $\text{M} = \text{Pb}(\text{II})$ ,  $\text{Mn}(\text{II})$ ,  $\text{Hg}(\text{II})$ , or  $\text{Zn}(\text{II})$ , and  $\text{X} = \text{Cl}$ ,  $\text{SO}_4$ , or  $\text{CH}_3\text{COO}$ ) and ethanolic solution of 4-(4-chlorophenyl)-1-(2-(phenylamino)acetyl)thiosemicarbazone, which have been previously reported [18]. The mixture was magnetically stirred at 60 °C for 6–8 h. The obtained precipitates were filtered, washed with anhydrous diethyl ether, and then dried under a vacuum in the presence of  $\text{P}_4\text{O}_{10}$  to afford the complexes ( $\text{B}_1$ – $\text{B}_4$ ), as shown in Scheme 1.

### 2.3. Physical Measurement

Elemental analyses (C, H, and N) were carried out at the Microanalytical Unit, Cairo University, Egypt. Metal content complexometric titration was estimated using EDTA following the standard literature methods, as reported by Basset et al. [19]. The FT-IR spectra were noted as KBr pellets using a Neneux-Nicolidite-640-MSAFT-IR spectrometer (4000–400  $\text{cm}^{-1}$ ). Mass spectra were acquired using the electron impact (EI) ionization technique at 70 eV using a Hewlett–Packard MS-5988 GC–MS instrument at the Microanalytical Center, National Research Centre, Dokki, Cairo, Egypt. The UV–visible absorption spectra were measured in an N, N-dimethylformamide (DMF) solution ( $10^{-3}$  M) using a 4802 UV/vis double beam spectrophotometer (Dayton, NJ, USA). The molar conductivity measurements were recorded using a Tacussel conductometer type CD6N in DMF solution ( $10^{-3}$  M). The magnetic properties of all complexes were recorded at room temperature by the modified Gouy method using a Magnetic Susceptibility Johnson Matthey Balance. The effective magnetic moments were calculated using the relation  $\mu_{\text{eff}} = 2.828 (X_m T)^{1/2}$  B.M., where  $X_m$  is the molar magnetic susceptibility corrected for diamagnetism of all atoms in the compounds using Selwood and Pascal's constants. Thermal analysis (TGA/DTG) was obtained by using a Shimadzu DTG-50 Thermal analyzer with a heating rate of 10 °C/min in a nitrogen atmosphere with the rate of 20 mL/min in a temperature range of 25–800 °C using platinum crucibles at the Central Lab, Faculty of Science, Menoufia University, Egypt. Using the Rigaku Model ROTAFLEX Ru-200, X-ray diffractograms of the solid samples were measured at the National Research Centre, Cairo, Egypt. Structural analysis of the X-ray diffractograms given by computer control formally was finished using a Philips X'Pert

MPD X-ray diffractometer ready with Cu radiation Cu K $\alpha$  ( $k = 1.54056 \text{ \AA}$ ). Usually, the most powder diffractometers use the Bragg–Brentano parafocusing geometry. The X-ray tube was utilized for a copper tube operating at 40 kV and 30 mA. The scanning range ( $2\theta$ ) was  $20\text{--}80^\circ$  with a step size of  $0.02^\circ$  and a counting time of 3 s/step. Quartz was used as the standard material to calibrate the instrumental extension. This identification of the complexes was done using the method described by Nair and Appukuttan [20] from the fit identified by the Scherrer formula; the average crystallite size,  $L$ , is measured as  $L = \lambda K / \beta \cos \theta$ , where  $\lambda$  is the X-ray wavelength in the monochromator,  $K$  is a constant equal to 0.9 related to crystallite shape, and  $\beta$  is the peak width at half maximum height. The value of  $\beta$  in the  $2\theta$  axis of the diffraction shape must be in radians. The  $\theta$  is the Bragg angle in radians since  $\cos \theta$  is compatible with the same number.



**Scheme 1.** Suggested chemical structures of the ligand (B) and metal complexes (B<sub>1</sub>–B<sub>4</sub>).

#### 2.4. Computational Study

In this part, we tried to discover the optimized geometrical parameters, such as bond lengths, bond angles, and net charges, on the coordinated atoms. The total energies (highest occupied molecular orbital (HOMO) energies, lowest unoccupied molecular orbital (LUMO) energies, and the dipole moments) for the ligand and complexes were computed. Density Functional Theory (DFT) at levels B3LYP, 6-311G, and LANL2DZ as the basis sets are used in all ligands and complexes calculations, respectively [21]. These calculations were carried out using G09W software [22]. All docking steps were done by Molecular Operating Environment (MOE 2008) software (Chemical Computing Group Inc., Montreal, QC, Canada) [23] to simulate the binding model of these compounds into an MK-2 enzyme (3WI6).

### 2.5. Irradiation Studies

For the irradiation studies, the solid samples of prepared compounds (B, B<sub>1</sub>, B<sub>2</sub>, B<sub>3</sub>, and B<sub>4</sub>) were subjected to a 60 kGy  $\gamma$ -irradiation dose with a rate equal to 2.2 kGy h<sup>-1</sup> [24]. The test was performed using the Indian <sup>60</sup>Co  $\gamma$ -ray cell type GE-4000 A at room temperature (at the Egyptian Atomic Energy Authority (EAEA), Nasr City, Egypt). After removing the samples from the radiation field, the FT-IR, absorption spectra, thermal analysis (TG/DTG), anti-bacterial, and anti-cancer activities of the irradiated samples were investigated. X-ray powder diffraction analyses of the un-irradiated (B, B<sub>2</sub>, and B<sub>4</sub>) and irradiated (A<sub>2</sub> and A<sub>4</sub>) samples of the synthesized compounds were conducted using a Rigaku Model ROTAFLEX Ru-200 at the National Research Centre, Dokki, Cairo, Egypt. The divergence and receiving slits values were 1 and 0.1, respectively.

### 2.6. Antimicrobial Assay

The antimicrobial activity of the synthesized compounds was determined using the disc-agar diffusion method [25] at the microanalytical unit of Cairo University, Egypt. The antimicrobial activity was performed against the sensitive organisms, including *Escherichia coli* (Gram-negative bacteria), *Staphylococcus aureus* (Gram-positive bacteria), *Aspergillus flavus* (fungi), and *Candida albicans* (fungi). Standard discs of ampicillin (antibacterial agent) and amphotericin B (antifungal agent) were served as positive controls for antimicrobial activity, while the filter discs impregnated with 10  $\mu$ L of the solvent dimethyl sulfoxide (DMSO) were used as a negative control. Briefly, 100  $\mu$ L of the test bacteria/fungi was grown in 10 mL of fresh media until they reached a count of approximately 10<sup>8</sup> cells/mL for bacteria or 10<sup>5</sup> cells/mL for fungi [26]. A total of 100  $\mu$ L of microbial suspension was spread onto agar plates corresponding to the broth, in which they were maintained. The plates were inoculated with filamentous fungi (*Aspergillus flavus*) at 25 °C for 48 h; Gram (+) bacteria (*Staphylococcus aureus*) and Gram (-) bacteria (*Escherichia coli*) were incubated at 35–37 °C for 24–48 h, and yeast (*Candida albicans*) incubated at 30 °C for 24–48 h. Subsequently, the diameters of the inhibition zones (in millimeters) were measured. Blank paper disks (Schleicher & Schuell, Spain, Sigma-Aldrich, St. Louis, MO, USA) with a diameter of 8.0 mm were impregnated with 10  $\mu$ L of the tested concentration of the stock solutions. When a filter paper disc, impregnated with a tested chemical, is placed on agar, the chemical will diffuse from the disc into the agar. This diffusion will locate the chemical in the agar only around the disc. Inhibition of the organisms, which is evidenced by the clear zone surrounding each disk, was measured and used to calculate the mean of the inhibition zone.

### 2.7. Cytotoxicity Assays

The cytotoxicity sample was prepared on cells by inoculating a 96-well tissue culture plate with 1  $\times$  10<sup>5</sup> cells/mL (100  $\mu$ L/well), incubated at 37 °C for 24 h, with washing media; the cell monolayer was washed twice to improve the complete monolayer sheet, and the growth medium was poured from 96-well microtiter plates after confluent sheet of cells were formed. Two-fold dilutions of the tested sample were prepared in Roswell Park Memorial Institute (RPMI) medium with 2% serum (maintenance medium). Then, 0.1 mL of each dilution was tested in different wells, leaving 3 wells as the control, receiving only a maintenance medium, and the plate was incubated at 37 °C and subsequently examined. Cells were checked for any actual indications of harmfulness, e.g., incomplete or complete loss of the monolayer, rounding, shrinkage, or cell granulation. The 3-(4,5-dimethylthiazol-2-yl)-2,5-diphenyl tetrazolium bromide (MTT) solution was prepared (5 mg/mL in PBS) (Bio Basic Inc., Markham, ON, Canada), and then 20  $\mu$ L MTT solution was added to each well. To thoroughly mix the MTT into the media, samples were incubated at 37 °C, 5% CO<sub>2</sub>, for 1–5 h to allow the MTT to be metabolized, and then placed on a shaking table at 150 rpm for 5 min, dumping off the media (to remove the dry residue on the paper towels if necessary). Formazan (MTT metabolic product) was resuspended in 200  $\mu$ L DMSO solution and placed on a shaking table at 150 rpm for 5 min to mix the formazan into the

solvent thoroughly. Finally, the optical density was recorded at 560 nm and the subtract background was measured at 620 nm. The optical density should be directly correlated with cell quantity [27,28].

### 3. Results and Discussion

#### 3.1. Physicochemical Properties

The experimental results showed that all the synthesized metal complexes are colored, stable in air, and insoluble in most organic solvents, except DMF and DMSO. The elemental analysis and physical data are summarized in Table 1. Elemental analyses indicate that the complexes (B<sub>1</sub>, B<sub>2</sub> and B<sub>4</sub>) are formed in a 1:2 (M:L) molar ratio while B<sub>3</sub> is formed in 2:1 (M:L). The analytical results agree well with the suggested formula. The molar conductivity in the 10<sup>-3</sup> M DMF solution indicated the non-electrolyte nature of the B<sub>1</sub> and B<sub>3</sub> complexes while showing the electrolyte nature of the B<sub>2</sub> and B<sub>4</sub> complexes [29].

**Table 1.** Analytical data of the ligand (H<sub>2</sub>L) and its metal complexes.

No.	Compounds	Color	Yield %	Mol. Wt.	Found (cal.) %					A <sub>m</sub>
					C	H	N	Cl	M	
B	H <sub>2</sub> L	Pale brown	75	334.5	53.43 (53.81)	4.46 (4.48)	16.47 (16.7)	10.83 (10.6)	—	—
B <sub>1</sub>	[Pb(H <sub>2</sub> L) <sub>2</sub> (OAc) <sub>2</sub> ]EtOH.H <sub>2</sub> O	White	75	1058.9	40.80 (40.8)	4.09 (4.16)	10.86 (10.58)	6.51 (6.70)	19.26 (19.57)	15
B <sub>2</sub>	[Mn(H <sub>2</sub> L)(HL)]Cl	Buff	81	758	48.05 (47.54)	3.36 (3.72)	13.7 (14.78)	13.87 (14.03)	6.89 (7.25)	77
B <sub>3</sub>	[Hg <sub>2</sub> (H <sub>2</sub> L)(OH)SO <sub>4</sub> ]	Buff	79	849.1	22.76 (21.22)	1.78 (1.90)	6.89 (6.60)	4.06 (4.18)	47.21 (47.25)	19
B <sub>4</sub>	[Zn(H <sub>2</sub> L)(HL)]Cl	Buff	86	768.46	46.82 (46.89)	3.65 (3.67)	14.53 (14.58)	13.81 (13.84)	8.50 (8.51)	76

Note: A<sub>m</sub> = molar conductivity (ohm<sup>-1</sup> cm<sup>2</sup> mol<sup>-1</sup>) in the 10<sup>-3</sup> M DMF solution.

#### 3.2. FT-IR

The FT-IR spectra of ligand H<sub>2</sub>L(B, A) and Pb(II), Mn(II), Hg(II) and Zn(II) complexes before and after  $\gamma$ -irradiation (B<sub>1</sub>–B<sub>4</sub> and A<sub>1</sub>–A<sub>4</sub>) are reported in Table 2, Figure 1, and Figure S1a–c. The FT-IR spectrum of the ligand before irradiation shows stretching frequencies of  $\nu$ (N4),  $\nu$ (N2),  $\nu$ (N1),  $\nu$ (C=O), and  $\nu$ (C=S) at 3335, 3302, 3100, 1670, and 750 cm<sup>-1</sup>, respectively. After  $\gamma$ -irradiation, the corresponding bands  $\nu$ (N4),  $\nu$ (N2),  $\nu$ (N1), and  $\nu$ (C=S) were shifted to higher wave numbers as compared to the free ligand. At the same time, the functional group of  $\nu$ (C=O) shifted to a lower wave number after  $\gamma$ -irradiation [30].

**Table 2.** Infrared spectral bands (cm<sup>-1</sup>) for the ligand (H<sub>2</sub>L) and their metal complexes.

No.	Compound	$\nu$ (N4)	$\nu$ (N2)	$\nu$ (N1)	$\nu$ (C=O)	$\nu$ (C=S)	$\nu$ (M-O)	$\nu$ (M-N)
B	H <sub>2</sub> L	3335	3302	3100	1670	750	—	—
A	H <sub>2</sub> L	3481	3302	3103	1668	751	—	—
B <sub>1</sub>	[Pb(H <sub>2</sub> L) <sub>2</sub> (OAc) <sub>2</sub> ]EtOH.H <sub>2</sub> O	3437	3242	3101	1667	756	508	625
A <sub>1</sub>	[Pb(H <sub>2</sub> L) <sub>2</sub> (OAc) <sub>2</sub> ]EtOH.H <sub>2</sub> O	3444	3296	3100	1672	755	468	548
B <sub>2</sub>	[Mn(H <sub>2</sub> L)(HL)]Cl	3461	3295	3134	1672	754	637	508
A <sub>2</sub>	[Mn(H <sub>2</sub> L)(HL)]Cl	3459	3295	3100	1672	755	637	507
B <sub>3</sub>	[Hg <sub>2</sub> (H <sub>2</sub> L)(OH)SO <sub>4</sub> ]	3378	3295	3104	1671	754	602	509
A <sub>3</sub>	[Hg <sub>2</sub> (H <sub>2</sub> L)(OH)SO <sub>4</sub> ]	3400	3291	2922	1670	754	606	510
B <sub>4</sub>	[Zn(H <sub>2</sub> L)(HL)]Cl	3450	3295	3102	1671	754	637	547
A <sub>4</sub>	[Zn(H <sub>2</sub> L)(HL)]Cl	3447	3295	3101	1671	754	637	550

Note: B = before  $\gamma$ -irradiation; A = after  $\gamma$ -irradiation.

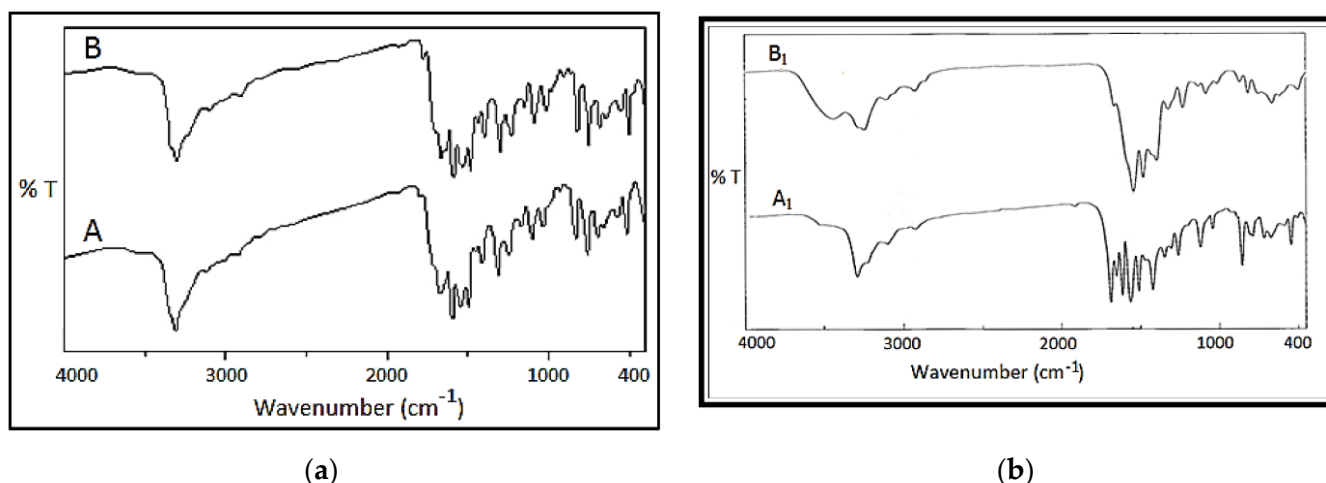


**Figure 1.** (a). FT-IR spectra of ligand before (B) and after (A) irradiation. (b) FT-IR spectra of the Pb (II) complexes before (B<sub>1</sub>) and after (A<sub>1</sub>) irradiation.

### 3.2.1. IR Spectra of the Pb(II) Complexes

The IR spectra of the Pb(II) complexes before and after  $\gamma$ -irradiation showed strong bands at 3437; 3442, 3242; 3296, 3101; 3100, 1667; 1672, and 756; 755  $\text{cm}^{-1}$  before and after  $\gamma$ -irradiation, which documented the stretching frequencies of the  $\nu(\text{N4})$ ,  $\nu(\text{N2})$ ,  $\nu(\text{N1})$ ,  $\nu(\text{C=O})$ , and  $\nu(\text{C=S})$  wagging vibrations, respectively. The IR spectra of the Pb(II) complexes before and after  $\gamma$ -irradiation were clear in that the band corresponding to  $\nu(\text{N1})$  and  $\nu(\text{C=S})$  are shifted to a lower frequency and the band corresponding to  $\nu(\text{N4})$ ,  $\nu(\text{N2})$ , and  $\nu(\text{C=O})$  are shifted to a higher frequency after  $\gamma$ -irradiation, with increasing sharper bands after  $\gamma$ -irradiation. The new bands appeared at 625; 548 and 508; 468  $\text{cm}^{-1}$ , assigned to  $\nu(\text{Pb-O})$  and  $\nu(\text{Pb-N})$ , respectively. Further, the Pb(II) complexes showed the additional stretching vibration band due to acetate at 1552 and 1595  $\text{cm}^{-1}$  before and after  $\gamma$ -irradiation, suggesting uncoordinated acetate ions.

Infrared spectra indicated that the intensity of the bands is sharper by using gamma rays [24].

### 3.2.2. IR Spectra of Mn(II) Complexes

The IR spectra of the Mn(II) complexes before and after  $\gamma$ -irradiation showed strong bands at 3461; 3459, 3295, 3134; 3100, 1672, and 754; 755  $\text{cm}^{-1}$ , which are attributed to the stretching frequencies of the  $\nu(\text{N4})$ ,  $\nu(\text{N2})$ ,  $\nu(\text{N1})$ ,  $\nu(\text{C=O})$ , and  $\nu(\text{C=S})$  wagging vibrations, respectively. It is clear that the band after  $\gamma$ -irradiation corresponding to  $\nu(\text{N4})$  and  $\nu(\text{N1})$  is shifted to a lower frequency, and the band corresponding to  $\nu(\text{C=S})$  is shifted to a higher frequency, which is sharper than the bands after  $\gamma$ -irradiation. The new bands appeared at 637; 508 and 507  $\text{cm}^{-1}$ , assigned to  $\nu(\text{Mn-O})$  and  $\nu(\text{Mn-N})$ , respectively.

### 3.2.3. IR Spectra of Hg (II) Complexes

The IR spectra of the Hg(II) complexes before and after irradiation showed strong bands at 3400, 3295; 3291, 3104, 1671; 1670, and 754  $\text{cm}^{-1}$ , which are ascribed to the stretching frequencies of the  $\nu(\text{N4})$ ,  $\nu(\text{N2})$ ,  $\nu(\text{N1})$ ,  $\nu(\text{C=O})$ , and  $\nu(\text{C=S})$  wagging vibrations, respectively. We observed that the band after  $\gamma$ -irradiation corresponding to  $\nu(\text{N4})$  is shifted to a higher frequency, while the band corresponding to  $\nu(\text{N2})$ ,  $\nu(\text{N1})$ , and  $\nu(\text{C=O})$  is shifted to a lower frequency, with increasing sharper bands after  $\gamma$ -irradiation. The new bands appeared at 602; 606 and 509; 510  $\text{cm}^{-1}$ , assigned to  $\nu(\text{Hg-O})$  and  $\nu(\text{Hg-N})$ , respectively, in addition to the  $\text{SO}_4$  group that appears at 1055 and 1054  $\text{cm}^{-1}$  before and after irradiation, respectively.

### 3.2.4. IR Spectra of Zn(II) Complexes

The IR spectra of the Zn(II) complexes before and after irradiation showed strong bands at 3450; 3447, 3295, 3102; 3101, 1671 and 754, 755  $\text{cm}^{-1}$ , which are attributed to the stretching frequencies of the  $\nu(\text{N4})$ ,  $\nu(\text{N2})$ ,  $\nu(\text{N1})$ ,  $\nu(\text{C=O})$ , and  $\nu(\text{C=S})$  wagging vibrations, respectively. We observed the band after  $\gamma$ -irradiation corresponding to  $\nu(\text{N4})$  and  $\nu(\text{N1})$  is shifted to a lower frequency and the band corresponding to  $\nu(\text{C=S})$  is shifted to a higher frequency, with sharper bands after  $\gamma$ -irradiation. The new bands appeared at 637; 547 and 550  $\text{cm}^{-1}$ , assigned to  $\nu(\text{Zn-O})$  and  $\nu(\text{Zn-N})$ , respectively.

### 3.3. Electronic Spectral Bands

The electronic spectral bands of the ligand and Pb(II), Mn(II), Hg(II), and Zn(II) complexes before (B, B<sub>1</sub>, B<sub>2</sub>, B<sub>3</sub>, and B<sub>4</sub>) and after (A, A<sub>1</sub>, A<sub>2</sub>, A<sub>3</sub>, and A<sub>4</sub>)  $\gamma$ -irradiation ( $\lambda_{\text{max}}$ , nm) in DMF solution in the range of 200–800 nm at room temperature are listed in Table 3 and Figure 2. UV spectra of the ligand (B and A) were perceived as the existence of two absorption bands at 260, 300, and 266, 303 nm before and after  $\gamma$ -irradiation, respectively, assigned to the  $\pi$ - $\pi^*$  transition. While, the UV-visible spectra of the Mn(II) complexes (B<sub>2</sub> and A<sub>2</sub>) before and after irradiation exhibited bands at 294, 292, 378, and 376 nm, respectively. The Zn(II) complexes (B<sub>4</sub> and A<sub>4</sub>) before and after irradiation also displayed bands at 291, 294, 375, and 378 nm, which may be assigned to  $n$ - $\pi^*$  transitions, representing a square planar geometry [31,32]. The electronic spectra of the Hg(II) complexes before and after irradiation (B<sub>3</sub> and A<sub>3</sub>) resulted in bands at 276, 281, 372, and 376 nm [33,34]. On the other side, the electronic spectra of the Pb(II) complexes (B<sub>1</sub> and A<sub>1</sub>) show three-bands at 270, 300, 320, and 354 nm assigned to  $n$ - $\pi^*$  transitions in an octahedral geometry around the Pb(II) ion, which is further confirmed by its diamagnetic nature [35,36]. The complexes showed no d-d band; the complexes contained only paired electrons and were diamagnetic.

After  $\gamma$ -irradiation, all peaks presented in the spectral diagram were observed. The difference between the electronic spectra of the ligand and its complexes in changing the value of the  $\lambda_{\text{max}}$  position and the value of absorbance were also investigated, indicating no change in the complexes' geometry; this result agrees with previous related studies. Irradiation can induce perturbation of energy levels as well as a deformity in the molecule [17].

**Table 3.** Electronic spectral data  $\lambda_{\text{max}}$  (nm) at room temperature of the ligand (H<sub>2</sub>L) and their metal complexes before and after irradiation.

No	Compounds	$\lambda_{\text{max}}$ (DMF, nm)
		Intra Ligand and Charge Transfer Bands
B	H <sub>2</sub> L	260, 300
A		266, 303
B <sub>1</sub>	[Pb(H <sub>2</sub> L) <sub>2</sub> (OAc) <sub>2</sub> ]EtOH.H <sub>2</sub> O	270, 300, 320
A <sub>1</sub>		270, 300, 354
B <sub>2</sub>	[Mn(H <sub>2</sub> L)(HL)]Cl	294, 378
A <sub>2</sub>		292, 376
B <sub>3</sub>	[Hg <sub>2</sub> (H <sub>2</sub> L)(OH)SO <sub>4</sub> ]	276, 372
A <sub>3</sub>		281, 376
B <sub>4</sub>	[Zn(H <sub>2</sub> L)(HL)]Cl	291, 375
A <sub>4</sub>		294, 378

### 3.4. PXRD of the Ligand and Metal Complexes

The X-ray diffractograms of the ligand (B) and the Mn(II) (B<sub>2</sub>, A<sub>2</sub>) and Zn(II) (B<sub>4</sub>, A<sub>4</sub>) complexes were evaluated (Table 4 and Figure 3 and Figure S2). The powder diffraction patterns were recorded over the  $2\theta = 5$ –90 range lattice constants. The intensities of the powder lines and the corresponding  $2\theta$  values are different for the irradiated samples, indicating the amorphous nature of the complex, whereas, upon irradiation, the sample

changed to crystalline materials. The average particle size of the crystalline structure of the ligand (B) and its complexes before and after irradiation was calculated using Scherer's equation [27,36]. The Scherer's constant (K) in the formula refers to the particle's shape, and it generally has a value of 0.9. It was found that the calculated crystalline size was in the nano range. The crystallite sizes were 35.12, 14.15, 32.59, 46.7, and 52.7 nm for the ligand, Mn(II), and Zn(II) unirradiated (B, B<sub>2</sub>, B<sub>4</sub>) and irradiated (A<sub>2</sub>, A<sub>4</sub>), respectively. The change in the size of the crystals may be due to the stress induced by the irradiation.

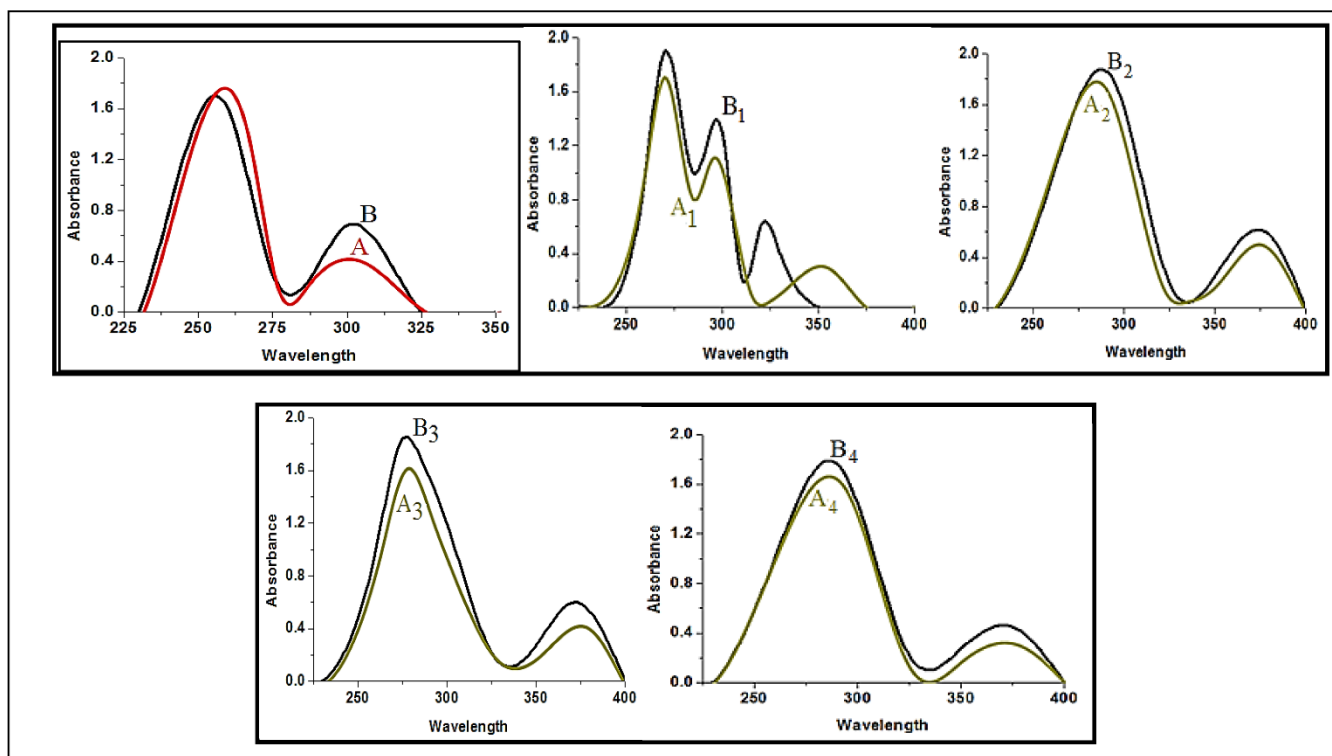


**Figure 2.** Electronic spectra of the synthesized Pb(II), Mn(II), Hg(II), and Zn(II) before (B, B<sub>1</sub>, B<sub>2</sub>, B<sub>3</sub>, and B<sub>4</sub>) and after (A, A<sub>1</sub>, A<sub>2</sub>, A<sub>3</sub>, and A<sub>4</sub>)  $\gamma$ -irradiation, respectively.

**Table 4.** PXRD data of the ligand Mn(II) and Zn(II) complexes before and after irradiation.

No	Compound	Angle 2 $\theta$	d-Value nm	FWHM	Grain Size nm
B	H <sub>2</sub> L	15.852	0.560592	0.215	41.50
		20.645	0.430118	0.256	35.12
		23.817	0.372922	0.220	41.02
B <sub>2</sub>	[Mn(H <sub>2</sub> L)(HL)]Cl	20.726	0.428912	0.202	44.52
		25.362	0.349939	0.319	28.40
		18.013	0.491038	0.632	14.15
A <sub>2</sub>	[Mn(H <sub>2</sub> L)(HL)]Cl	20.692	0.429487	0.199	45.15
		22.228	0.399270	0.276	32.59
		26.170	0.340655	0.208	43.51
B <sub>4</sub>	[Zn(H <sub>2</sub> L)(HL)]Cl	20.652	0.429736	0.016	74.8
		26.658	0.334125	0.030	46.7
		27.211	0.327455	0.015	79.8
A <sub>4</sub>	[Zn(H <sub>2</sub> L)(HL)]Cl	22.245	0.399307	0.021	59.3
		26.171	0.340227	0.019	63.9
		28.512	0.339015	0.025	52.7

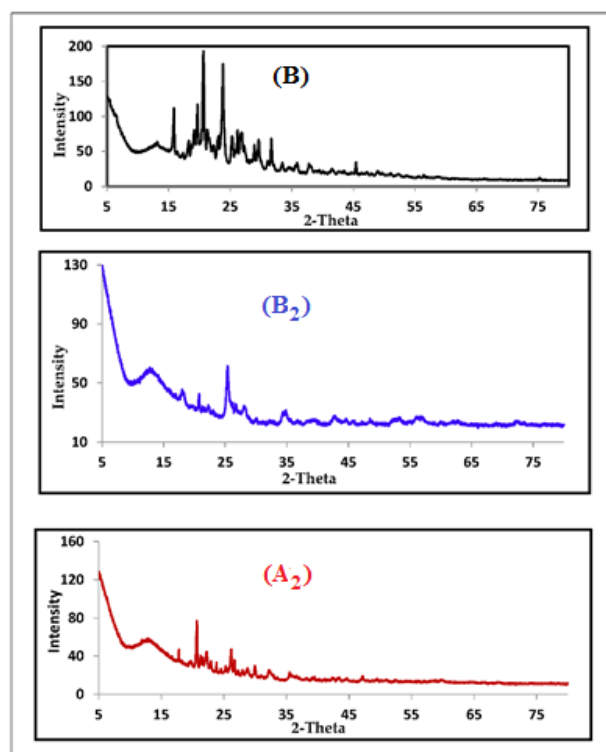


**Figure 3.** PXR D powder pattern of the ligand (B) and Mn(II) complex before (B, B<sub>2</sub>) and after irradiation (A<sub>2</sub>).

### 3.5. Mass Spectra

The mass spectra were mainly performed to confirm the composition and support the structure of the synthesized chelates. The molecular ion peaks for the Hg(II) complex were examined at  $m/z = 849.1$  (Table 1 and Figure 4), which suggests the stoichiometry of the metal and ligand in metal chelates as a 2:1 ratio. The observed data of the complexes are in agreement with their formula as designated from the microanalytical data.

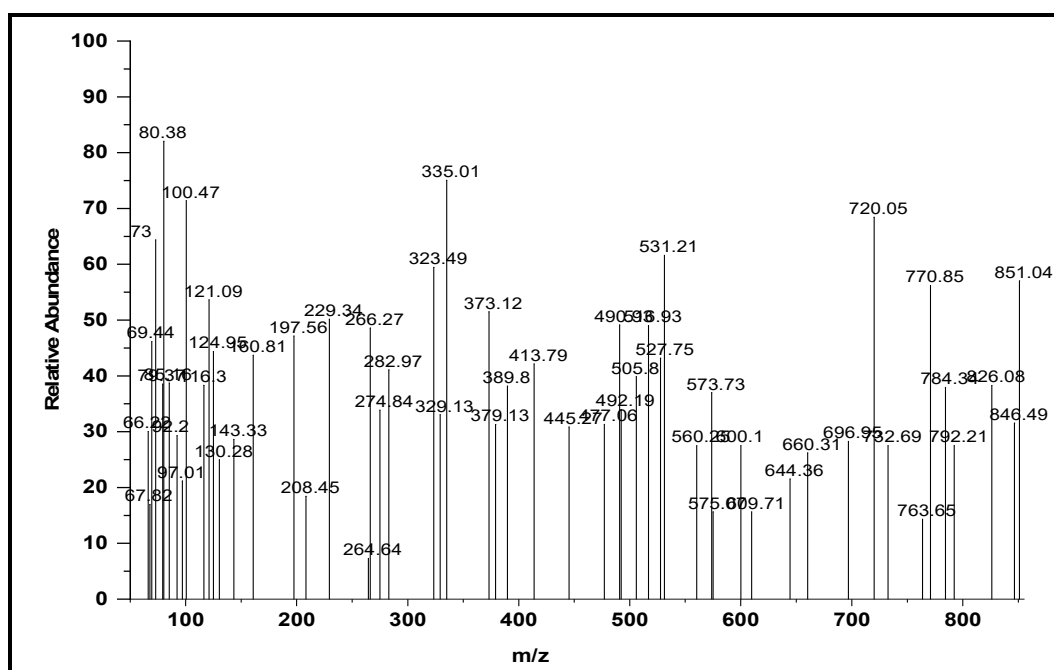


**Figure 4.** The mass spectrum of the Hg(II) complexes.

The proposed structures of the complexes were established from analytical and multi spectroscopic methods (Scheme 1).

### 3.6. Thermal Analysis

The thermal behavior of the ligand (B, A) and Pb(II) (B<sub>1</sub>, A<sub>1</sub>), Mn(II) (B<sub>2</sub>, A<sub>2</sub>), Hg(II) (B<sub>3</sub>, A<sub>3</sub>), and Zn(II) (B<sub>4</sub>, A<sub>4</sub>) complexes before and after  $\gamma$ -irradiation are listed in Table 5 and Figure 5a–e. The TG curves of B and A in Figure 5a revealed thermal stability till 190 °C and 240 °C, and also showed two decomposition steps in a temperature range of 190–633 °C and 240–680 °C, with the total weight loss of calc. 99.9% (found 100%) and calc. 100% (found 100%) before and after  $\gamma$ -irradiation, respectively. After irradiation, the thermogravimetric analyses (TG) curves of the ligand revealed that  $\gamma$ -irradiation stimulated more thermal stability of the substance than those that were un-irradiated. These results are consistent with the structure of the ligand resolute as determined by the elemental analysis and IR spectroscopy.

**Table 5.** Thermal data of the ligand and its metal complexes.

No	Compound	TAG(A)/°C	Wt. Loss Calc. (Found) %	Leaving Species
B	H <sub>2</sub> L	At 190 190–633	- 99.9	Melting Gradual decomp.
A	H <sub>2</sub> L	At 190 240–680	- 100	melting Gradual decomp.
B <sub>1</sub>	[Pb(H <sub>2</sub> L) <sub>2</sub> (OAc) <sub>2</sub> ]EtOH.H <sub>2</sub> O	30–125 395–548 >719.30	6.05 (6.15) 74.39 (74.29) 19.57 (19.54)	EtOH + H <sub>2</sub> O C <sub>34</sub> H <sub>36</sub> Cl <sub>2</sub> N <sub>8</sub> O <sub>6</sub> S <sub>2</sub> Pb
A <sub>1</sub>	[Pb(H <sub>2</sub> L) <sub>2</sub> (OAc) <sub>2</sub> ]EtOH.H <sub>2</sub> O	30–125 395–548 >719.30	6.05 (6.15) 74.39 (74.29) 19.57 (19.54)	EtOH + H <sub>2</sub> O C <sub>34</sub> H <sub>36</sub> Cl <sub>2</sub> N <sub>8</sub> O <sub>6</sub> S <sub>2</sub> Pb
B <sub>2</sub>	Mn(H <sub>2</sub> L)(HL)]Cl	170–402 436–553 719–791 >791	62.34 (62.31) 13.19 (13.22) 11.35 (11.32) 13.05 (13.15)	C <sub>24</sub> H <sub>22</sub> Cl <sub>3</sub> N <sub>4</sub> C <sub>3</sub> H <sub>4</sub> N <sub>2</sub> S C <sub>2</sub> H <sub>2</sub> N <sub>2</sub> S MnO + CO
A <sub>2</sub>	[Mn(H <sub>2</sub> L)(HL)]Cl	172–329 350–652 >652	77.64 (77.62) 9.23 (9.21) 13.05 (13.20)	C <sub>28</sub> H <sub>26</sub> Cl <sub>3</sub> N <sub>4</sub> S <sub>2</sub> CH <sub>2</sub> N <sub>4</sub> MnO + CO
B <sub>3</sub>	[Hg <sub>2</sub> (H <sub>2</sub> L)(OH)SO <sub>4</sub> ]	117–194 194–287 296–421 429–615 >615	32.68 (32.65) 1.64 (1.60) 11.30 (11.32) 3.53 (3.55) 51.07 (51.05)	C <sub>14</sub> H <sub>14</sub> ClN <sub>2</sub> S CH <sub>2</sub> SO <sub>4</sub> NO 2HgO
A <sub>3</sub>	[Hg <sub>2</sub> (H <sub>2</sub> L)(OH)SO <sub>4</sub> ]	119–230 230–303 309–446 454–640 >640	32.68 (32.65) 1.64 (1.60) 11.30 (11.32) 3.53 (3.55) 51.07 (51.05)	C <sub>14</sub> H <sub>14</sub> ClN <sub>2</sub> S CH <sub>2</sub> SO <sub>4</sub> NO 2HgO
B <sub>4</sub>	[Zn(H <sub>2</sub> L)(HL)]Cl	152–356 482–652 733–799 >799	55.76 (55.74) 22.94 (22.92) 5.47 (5.50) 15.80 (15.78)	C <sub>23</sub> H <sub>18</sub> N <sub>2</sub> Cl <sub>3</sub> C <sub>4</sub> H <sub>8</sub> N <sub>4</sub> S <sub>2</sub> CH <sub>2</sub> N <sub>2</sub> Zn + 2CO
A <sub>4</sub>	[Zn(H <sub>2</sub> L)(HL)]Cl	152–356 482–652 733–799 >799	55.76 (55.74) 22.94 (22.92) 5.47 (5.50) 15.80 (15.78)	C <sub>23</sub> H <sub>18</sub> N <sub>2</sub> Cl <sub>3</sub> C <sub>4</sub> H <sub>8</sub> N <sub>4</sub> S <sub>2</sub> CH <sub>2</sub> N <sub>2</sub> Zn + 2CO

Figure 5b shows that the TG curves of the Pb(II) complexes before  $B_4$  and after  $A_4$   $\gamma$ -irradiation exhibited weight loss calc. 6.047% (found 6.75%) at a temperature range of 30–125 °C, attributed to losing one molecule of water and ethanol on one step. On further heating, the complexes decomposed at 245–548 °C. The final stage ended with the remaining Pb as the final residue. After  $\gamma$ -irradiation, the TG curve of ( $A_4$ ) was similar to ( $B_4$ ) before  $\gamma$ -irradiation.

Figure 5c shows TG curves for the Mn(II) complexes before  $B_1$  and after  $A_1$   $\gamma$ -irradiation. The TG curves of  $B_1$  exhibited three degradation stages; the first stage in a temperature range of 170–402 °C exhibited weight loss (calc./found % 62.34/62.31) allocated to the loss of the  $C_{24}H_{22}Cl_3N_4$  moiety. The second stage in a temperature range of 436–553 °C (calc./found % 13.19/13.22) was correlated with the loss of the  $C_3H_4N_2S$  moiety. The third stage in a temperature range of 719–791 °C (calc./found % 11.35/11.32) corresponded to the loss of the  $C_2H_2N_2S$  moiety, leaving species MnO + CO in the fourth stage as the final remainder over at 791 °C. Moreover, the TG curve of  $A_1$  displayed three degradation stages; the first stage in a temperature range of 172–329 °C exhibited weight loss (calc./found % 77.64/77.62) that was allocated to the loss of the  $C_{28}H_{26}Cl_3N_4S_2$  moiety. The second stage in a temperature range of 350–652 °C (calc./found % 9.23/9.21) corresponded to the loss of the  $CH_2N_4$  moiety, leaving species of MnO + CO in the third stage as the final remainder over at 652 °C.

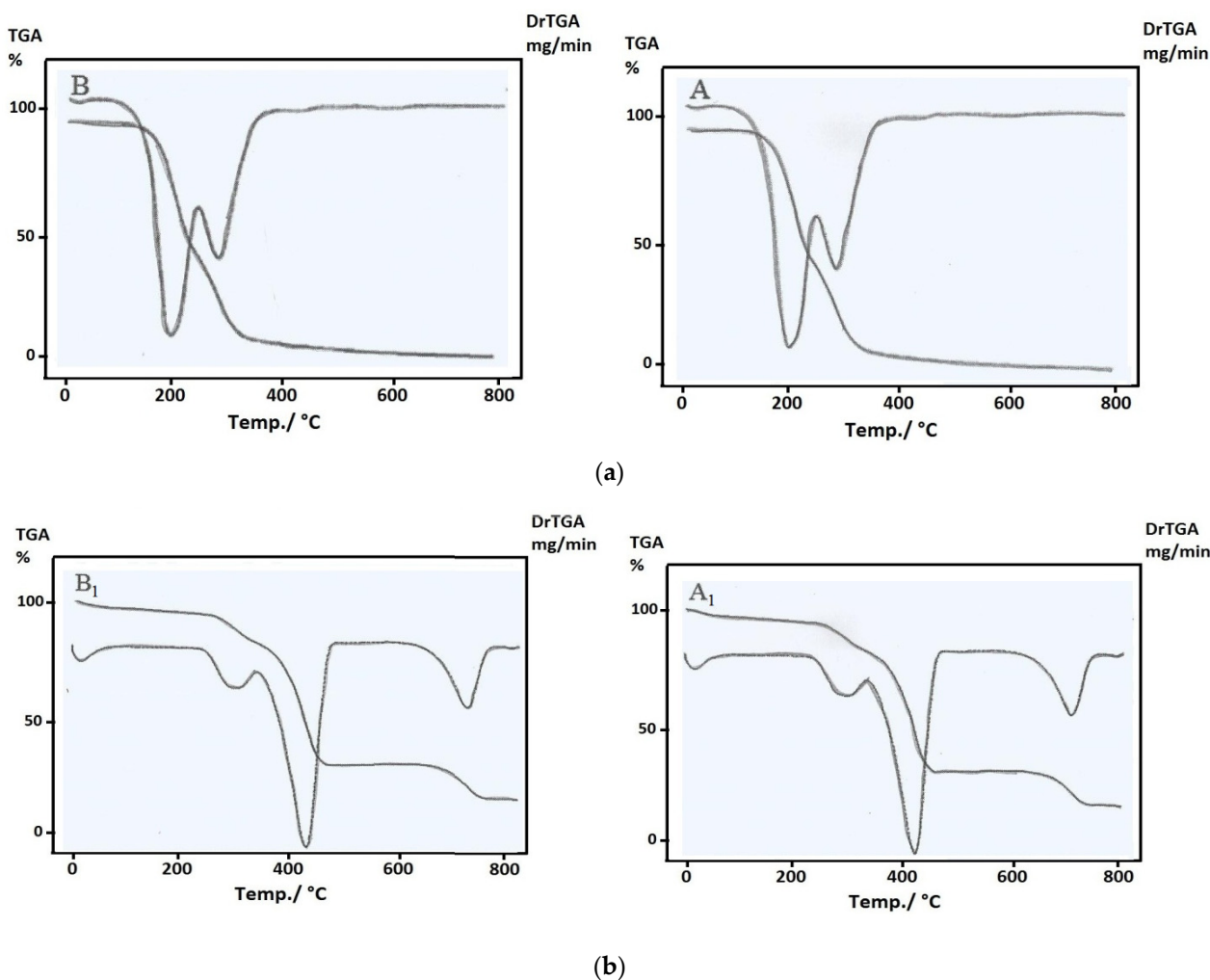
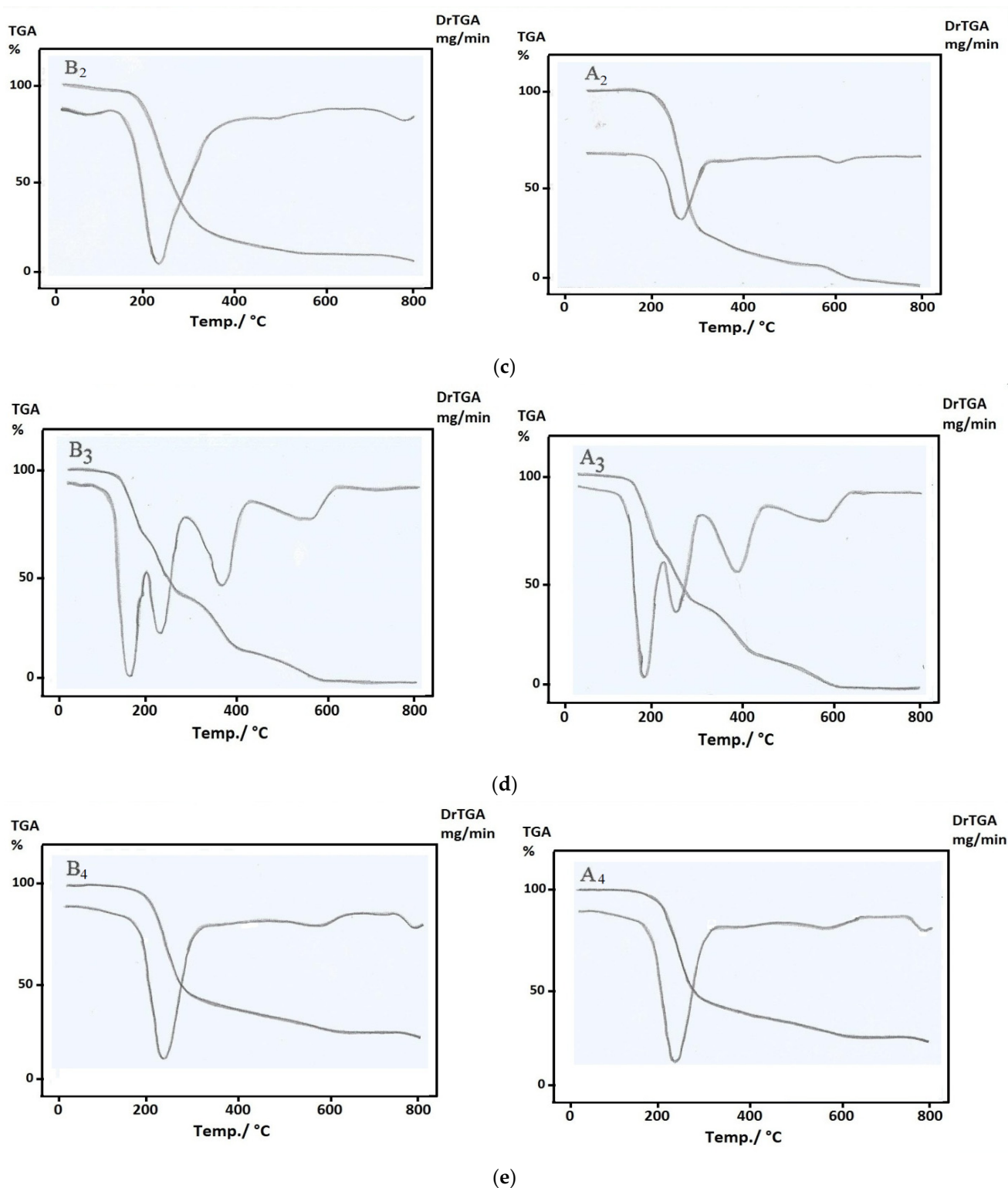


Figure 5. Cont.



**Figure 5.** (a). TGA/DTG curves of the ligand before (B) and after (A) irradiation. (b) TGA/DTG curves of the Pb(II) complexes before irradiation (B<sub>1</sub>) and after irradiation (A<sub>1</sub>). (c). TGA/DTG curves of the Mn(II) complexes before irradiation (B<sub>2</sub>) and after irradiation (A<sub>2</sub>). (d). TGA/DTG curves of the Hg(II) complexes before irradiation (B<sub>3</sub>) and after irradiation (A<sub>3</sub>). (e). TGA/DTG curves of Zn(II) complexes before irradiation (B<sub>4</sub>) and after irradiation (A<sub>4</sub>).

Figure 5d shows TG curves for the Hg(II) complexes before B<sub>3</sub> and after A<sub>3</sub>  $\gamma$ -irradiation. The TG curve of B<sub>3</sub> exhibited five degradation stages; the first exhibited weight loss (calc./found % 32.68/32.65) in a temperature range of 117–194 °C, which was

allocated to the loss of the  $C_{14}H_{14}ClN_2S$  moiety. The second stage in a temperature range of 194–287 °C (Calc./Found % 1.64/1.60) corresponded to the loss of  $CH_2$ . In addition, the third stage in a temperature range 296–421 °C (calc./found % 11.30/11.32) was correlated with the loss of  $SO_4$ . The fourth stage in a temperature range of 429–615 °C (calc./found % 3.53/3.55) corresponded to the loss of  $NO$ , leaving metal oxide ( $2HgO$ ) as the final residue over at 615 °C. The TG curve after irradiation  $A_3$  was similar to before irradiation  $B_3$ , with a different extent of dissociation.

Figure 5e shows TG curves for the Zn(II) complexes before  $B_2$  and after  $A_2$   $\gamma$ -irradiation. It observed that the TG curves of  $B_2$  were similar to that of  $A_2$ , and both of them exhibited four degradation stages; the first stage exhibited weight loss (calc./found % 55.76/55.74) in a temperature range of 152–356 °C, which was allocated to the loss of the  $C_{23}H_{18}N_2Cl_3$  moiety. The second stage in a temperature range of 482–652 °C (calc./found % 22.94/22.92) corresponds to the loss of the  $C_4H_8N_4S_2$  moiety. While, the third stage in a temperature range of 733–799 °C (calc./found % 5.47/5.50) was correlated with the loss of the  $CH_2N_2$  moiety, leaving  $Zn + 2CO$  in the fourth stage as the final remainder over at 799 °C.

### 3.7. DFT Calculations of the Ligand and Metal Complexes

The natural charges, obtained from Natural Bond Orbital Analysis (NBO), showed that the more negative active sites were in the following order: S14 (−0.29189) < N12 (−0.40986) < O10 (−0.65733). Thus, the metal ions preferred the coordination through O10, N12, or S14, forming membered rings.

Figure S3 shows the optimized structures of the ligand and metal complexes as the lowest energy configurations. The lead atom is six-coordinate in an octahedral geometry by using the S14, N12, and O-acetate donor atoms. However, the other metal complexes were optimized in tetrahedral shapes using the most electron-donating atoms S14 and N12. Many bond lengths were elongated after coordination that supported the coordination through the previously mentioned donor sites. Some of these bond lengths were elongated, such as R(C13-N15), R(N12-C13), R(N12-N11), R(C9-O10), and R(C8-N7) [37]. The polarity of ligand increased after complexation by its coordination with metal ions, as indicated from the magnitude of their dipole moments. The ionic complexes have higher polarity than the non-electrolytic complexes. The natural charges computed from the NBO analysis on the coordinated atoms are observed in Table 6 as Hg (+0.852), Mn(+0.650), Pb(+1.678), and Zn(+1.031). For donor centers, the examined ligand was changed to less negative values, as [S14(−0.048), N12(−0.217), O10(−0.404), and O24(−0.830)] in the Hg chelate; [N12(−0.320) and O10(−0.404)] in the Mn chelate; [N12(−0.367), O10(−0.497), and O47(−0.616)] in the Pb chelate; and [N12(−0.335) and O10(−0.461)] in the Zn chelate. Thus, it can be explained due to the charge transfer from the examined ligand donor sites to the central metal ions, i.e., L→M. Table 7 shows some of the optimized bond lengths (Å) and bond angles (degrees) for  $H_2L$  and the complexes using B3LYP/6-311G. The coordinates of the optimized ligand and complexes are tabulated in Tables S1–S5.

**Table 6.** Atomic charges in terms of the natural population analysis (NPA) of the  $H_2L$  ligand and its metal complexes using B3LYP/6-311G and B3LYP/LANL2DZ, respectively.

Element	NPA				
	B	B <sub>1</sub>	B <sub>2</sub>	B <sub>3</sub>	B <sub>4</sub>
M	—	1.67821	0.65011	0.85211	1.03112
C1	−0.18056	−0.18135	−0.18756	−0.19196	−0.19057
C2	−0.24771	−0.24394	−0.23325	−0.25448	−0.25331
C3	−0.17807	−0.19254	−0.18283	−0.20104	−0.19577
C4	−0.28054	−0.25886	−0.25336	−0.31010	−0.26045

Table 6. Cont.

Element	NPA				
	B	B <sub>1</sub>	B <sub>2</sub>	B <sub>3</sub>	B <sub>4</sub>
C5	0.18087	0.18822	0.17412	0.18013	0.19940
C6	−0.24826	−0.28885	−0.30542	−0.25276	−0.29428
N7	−0.60338	−0.66805	−0.69606	−0.67381	−0.66249
C8	−0.25744	−0.26038	−0.26700	−0.27733	−0.26293
C9	0.64369	0.69298	0.71808	0.75303	0.70812
O10	−0.65733	−0.49713	−0.40412	−0.40412	−0.46111
N11	−0.41815	−0.39751	−0.38941	−0.50338	−0.42824
N12	−0.40986	−0.36714	−0.32029	−0.21712	−0.33512
C13	0.28170	0.30768	0.24750	0.36903	0.28989
S14	−0.29189	−0.26236	−0.13222	−0.04822	−0.30757
N15	−0.58636	−0.63000	−0.62512	−0.64017	−0.66131
C16	0.15363	0.16474	0.25552	0.16215	0.15459
C17	−0.20568	−0.19422	−0.22200	−0.21503	−0.20142
C18	−0.22105	−0.22251	−0.14183	−0.20965	−0.20639
C19	−0.00103	0.00409	−0.02894	−0.00010	−0.00416
C20	−0.21685	−0.22700	−0.14384	−0.21398	−0.21251
C21	−0.18693	−0.20328	−0.37396	−0.21795	−0.25495
Cl22	−0.03812	−0.06190	−0.02117	−0.04121	−0.07127
O47-Ac	—	−0.61622	—	—	—
C49	—	0.84717	—	—	—
O51	—	−0.56608	—	—	—
C53	—	−0.73832	—	—	—
O24	—	—	—	−1.20638	—
O26	—	—	—	−1.04297	—
O27	—	—	—	−0.97943	—
S28	—	—	—	2.14241	—

Table 7. Some of the optimized bond lengths (Å) and bond angles (degrees) for H<sub>2</sub>L and the complexes using B3LYP/6-311G.

Bond Length (Å)	H <sub>2</sub> L	[Pb(H <sub>2</sub> L) <sub>2</sub> (OAc) <sub>2</sub> ]·EtOH·H <sub>2</sub> O	[Mn(H <sub>2</sub> L)(HL)]Cl	[Hg <sub>2</sub> (H <sub>2</sub> L)(OH)SO <sub>4</sub> ]	[Zn(H <sub>2</sub> L)(HL)]Cl
R(Hg23-S14)	—	—	—	2.69	—
R(Hg23-N12)	—	2.19	1.99	2.37	2.07
R(Hg23-O10)	—	2.22	1.90	2.68	2.03
R(Hg23-O24)	—	—	—	2.18	—
R(Mn-O32)	—	2.21	1.99	—	2.02588
R(Mn-N34)	—	2.25	1.82	—	2.08
R(Hg25-O27)	—	—	—	2.26	—
R(Hg25-O26)	—	—	—	2.27	—
R(Pb-O47)	—	2.02	—	—	—
R(S28-O26)	—	—	—	1.76	—
R(S28-O27)	—	—	—	1.75	—
R(C13-S14)	1.73	1.73	1.72	1.82	1.76

Table 7. Cont.

Bond Length (Å)	H <sub>2</sub> L	[Pb(H <sub>2</sub> L) <sub>2</sub> (OAc) <sub>2</sub> ]ETOH.H <sub>2</sub> O	[Mn(H <sub>2</sub> L)(HL)]Cl	[Hg <sub>2</sub> (H <sub>2</sub> L)(OH)SO <sub>4</sub> ]	[Zn(H <sub>2</sub> L)(HL)]Cl
R(C13-N15)	1.37	1.37	1.40	1.36	1.38
R(N12-C13)	1.36	1.39	1.38	1.35	1.38
R(N12-N11)	1.39	1.40	1.41	1.42	1.42
R(N11-C9)	1.36	1.33	1.33	1.38	1.34
R(C9-O10)	1.26	1.31	1.32	1.27	1.30
R(C8-N7)	1.44	1.45	1.44	1.44	1.45
A(S14-C13-N12)	—	—	—	112.84	—
A(O10-C9-N11)	—	119.52	116.63	119.34	119.91
A(O24-Hg23-O10)	—	—	—	73.30	—
A(O24-Hg25-O10)	—	—	71.99	75.00	—
A(O27-Hg25-O26)	—	—	98.36	70.03	—
A(O27-S28-O26)	—	—	125.40	95.80	—
A(N12-Mn-O10)	—	74.54	80.42	—	81.16
A(O32-Mn-N34)	—	76.39	82.87	—	80.97
A(O10-Pb-N34)	—	106.17	—	66.77	126.95

The theoretically calculated frontier molecular orbitals in the ground state are illustrated in Figure 6. The global reactivity descriptors, such as the ionization potential (I), electron affinity (A), absolute electronegativity ( $\chi$ ), absolute hardness ( $\eta$ ), and softness (S), for the molecule were calculated at the same levels, and the results are presented in Table 8. These molecular properties can be calculated as follows: hardness,  $\eta = (I - A)/2$ ; softness (S),  $S = 1/2\eta$ ; chemical potential ( $\mu$ ),  $\mu = -(I + A)/2$ ; and electronegativity ( $\chi$ ),  $\chi = (I + A)/2$ .

The lower value of the energy gap explains the charge transfer interactions taking place within the molecule, which influences the molecule's biological activity. The energy gap reflects the chemical activity of the molecule. A molecule with a small frontier orbital gap is generally associated with a high chemical reactivity and is defined as a soft molecule.

Table 8. Ground state properties of the H<sub>2</sub>L ligand using B3LYP/6-31G and its metal complexes using B3LYP/LANL2DZ.

Parameter	H <sub>2</sub> L	[Pb(H <sub>2</sub> L) <sub>2</sub> (OAc) <sub>2</sub> ]ETOH.H <sub>2</sub> O	[Mn(H <sub>2</sub> L)(HL)]Cl	[Hg <sub>2</sub> (H <sub>2</sub> L)(OH)SO <sub>4</sub> ]	[Zn(H <sub>2</sub> L)(HL)]Cl
E <sub>T</sub> , Hartree	-1733.21933	-2258.72234	-1902.06064	-1371.26441	-1864.02372
E <sub>HOMO</sub> , eV	-5.94	-5.52	-6.38	-5.51	-2.67
E <sub>LUMO</sub> , eV	-5.43	-4.82	-5.82	-3.92	-2.44
ΔE, eV	0.51	2.53	1.0	1.59	0.416
I = -E <sub>HOMO</sub> , eV	5.94	5.52	6.38	5.51	2.67
A = -E <sub>LUMO</sub> , eV	5.43	4.82	5.82	3.92	2.44
χ, eV	22.27	14.77	21.78	5.92	22.17
η, eV	0.255	0.35	0.28	0.795	0.115
S, eV <sup>-1</sup>	1.96	1.42	1.78	0.62	4.34
μ, eV	-5.68	-5.17	-6.10	-4.71	-2.55
Dipole Moment (Debye)	2.41	7.65	6.96	19.90	6.11

Note: E: the total energy (a.u.); HOMO: highest occupied molecular orbital (eV); and LUMO: lowest unoccupied molecular orbital (eV). ΔE = E<sub>LUMO</sub> - E<sub>HOMO</sub>.

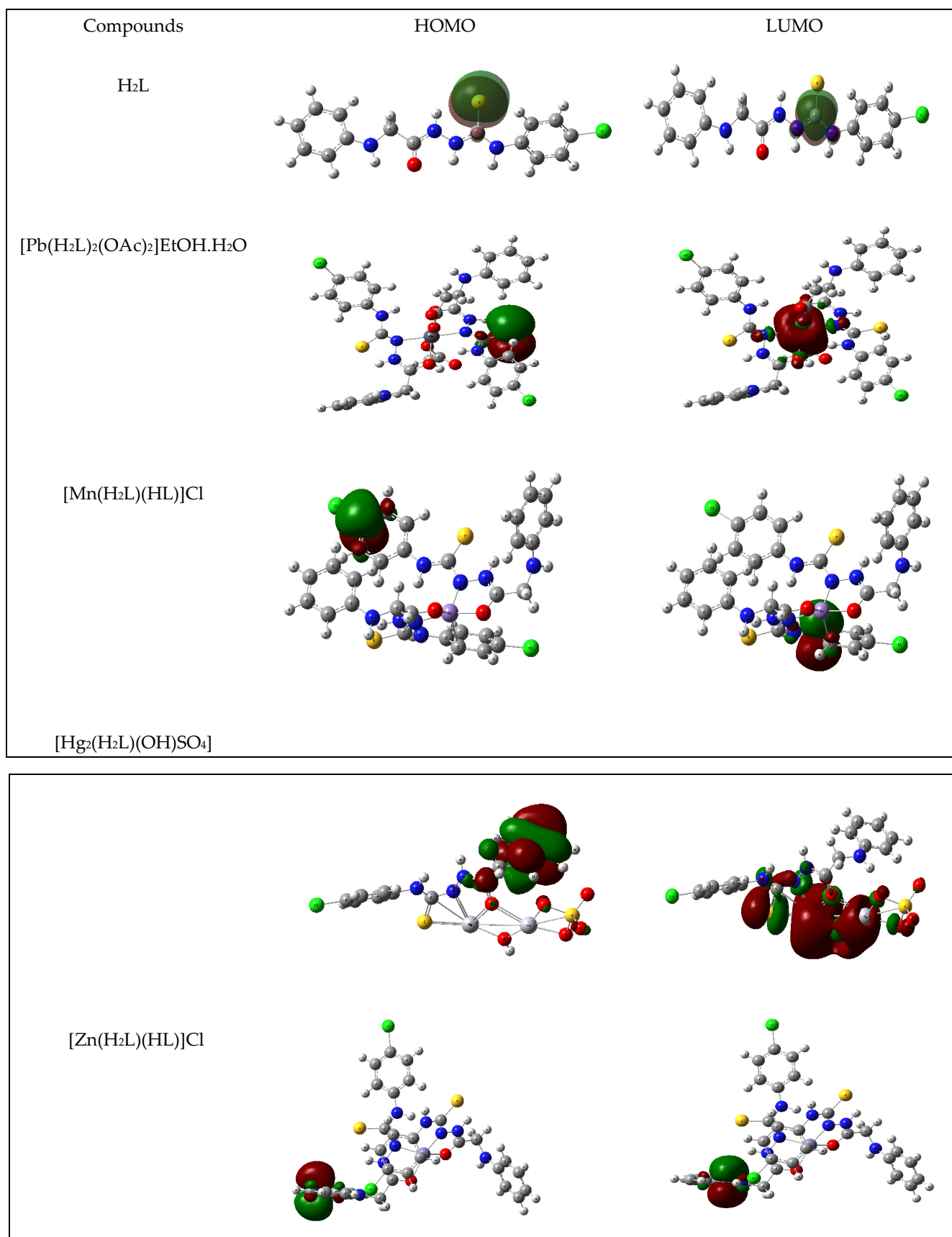


**Figure 6.** Frontier HOMO and LUMO molecular orbitals for the ligand H<sub>2</sub>L and Pb(II), Mn(II), Hg(II), and Zn(II) complexes, calculated at DFT level.

### 3.8. Biological Applications

#### 3.8.1. Antimicrobial Activity

The thiosemicarbazide ligand and chelate compounds before and after irradiation had varying degrees of inhibitory effect on the growth of Gram-negative bacteria, such as *Escherichia coli*, *Klebsiella pneumonia*, and *Pseudomonas aeruginosa*, Gram-positive bacteria (*Staphylococcus aureus* and *Streptococcus mutans*), and fungi (*Candida albicans* and *Aspergillus Nigar*); the inhibitory effect results are presented in Table S6 and Figure 7. Furthermore, *C. albicans* was affected by complex (B<sub>3</sub>, B<sub>4</sub>) before irradiation, with inhibition ranges of  $10.3 \pm 0.5$  and  $23.6 \pm 0.6$ , respectively. In turn, complex (A<sub>3</sub>) after irradiation showed higher activity, with an inhibition range of  $31.6 \pm 0.6$ . *A. nigar* was affected by complex (B<sub>3</sub>) before irradiation, with an inhibition range of  $29.3 \pm 0.6$ , and the higher activity was for complex (A<sub>3</sub>) after irradiation, with an inhibition range of  $30.6 \pm 0.6$ ; this is compared with the positive control drug used for both fungi. The in vitro antimicrobial activity exhibited by the synthesized compounds before and after irradiation is in Table S6. The results showed that complex (B<sub>3</sub>) before irradiation towards Gram-negative bacteria (*E. coli*, *K. pneumonia*, and *P. aeruginosa*) had higher activity than other complexes, with an inhibition range of  $23.3 \pm 0.6$ ,  $22.6 \pm 0.6$ , and  $21.3 \pm 0.6$ , respectively. The complex (A<sub>3</sub>) after irradiation had the highest activity, with an inhibition range of  $29.6 \pm 0.6$ ,  $20.6 \pm 0.6$ , and  $27.6 \pm 0.6$ , respectively, compared with other complexes before and after irradiation. In addition, the results reported that complex (A<sub>3</sub>) after irradiation had the highest activity with an inhibition range of  $33.3 \pm 0.6$  and  $19.6 \pm 0.6$ , while complex (B<sub>3</sub>) before irradiation towards Gram-positive bacteria (*S. aureus* and *S. mutans*) had higher activity than other complexes, with an inhibition range of  $36.6 \pm 0.6$  and  $28.6 \pm 0.6$ , respectively. Therefore, the [Hg<sub>2</sub>(H<sub>2</sub>L)(OH)SO<sub>4</sub>] complex after irradiation had a higher activity than other complexes. These results can be demonstrated according to the basis of Overtone's concept and Tweedy's chelation theory [38–41], as the chelation increases the delocalization of p-electrons over the whole ring. Hence, this enhances the compounds' penetration into lipid membranes. In addition, the oxidation state of the metal ion, type, and number of donor sites besides their relative presence within the ligand, solubility, conductivity, particle size, and bond length between the metal and ligand are also important in determining the antimicrobial activity of compounds [42,43].

#### 3.8.2. Cytotoxicity

The cytotoxic activities of the ligand and their complexes before and after irradiation were evaluated against the human liver cancer cell line (HepG2) and normal cell line (HEK-293), as presented in Table 9, Figure 8, and Figure S4. The results are expressed as the IC<sub>50</sub>, which is the concentration of a drug that causes a 50% reduction in the proliferation of cancer cells when compared to the growth of the control cells. The thiosemicarbazide ligand before irradiation (B) was more biologically active than after irradiation (A), where the IC<sub>50</sub> value of B is 20.45, while A is 29.25. The Mn(II) and Zn(II) complexes after irradiation (A<sub>2</sub>, A<sub>4</sub>) against the human liver HepG2 cancer are more effective than the Mn(II) and Zn(II) complexes before irradiation (B<sub>2</sub>, B<sub>4</sub>). Moreover, (A<sub>2</sub>, A<sub>4</sub>) had lower IC<sub>50</sub> values than (B<sub>2</sub>, B<sub>4</sub>), respectively.

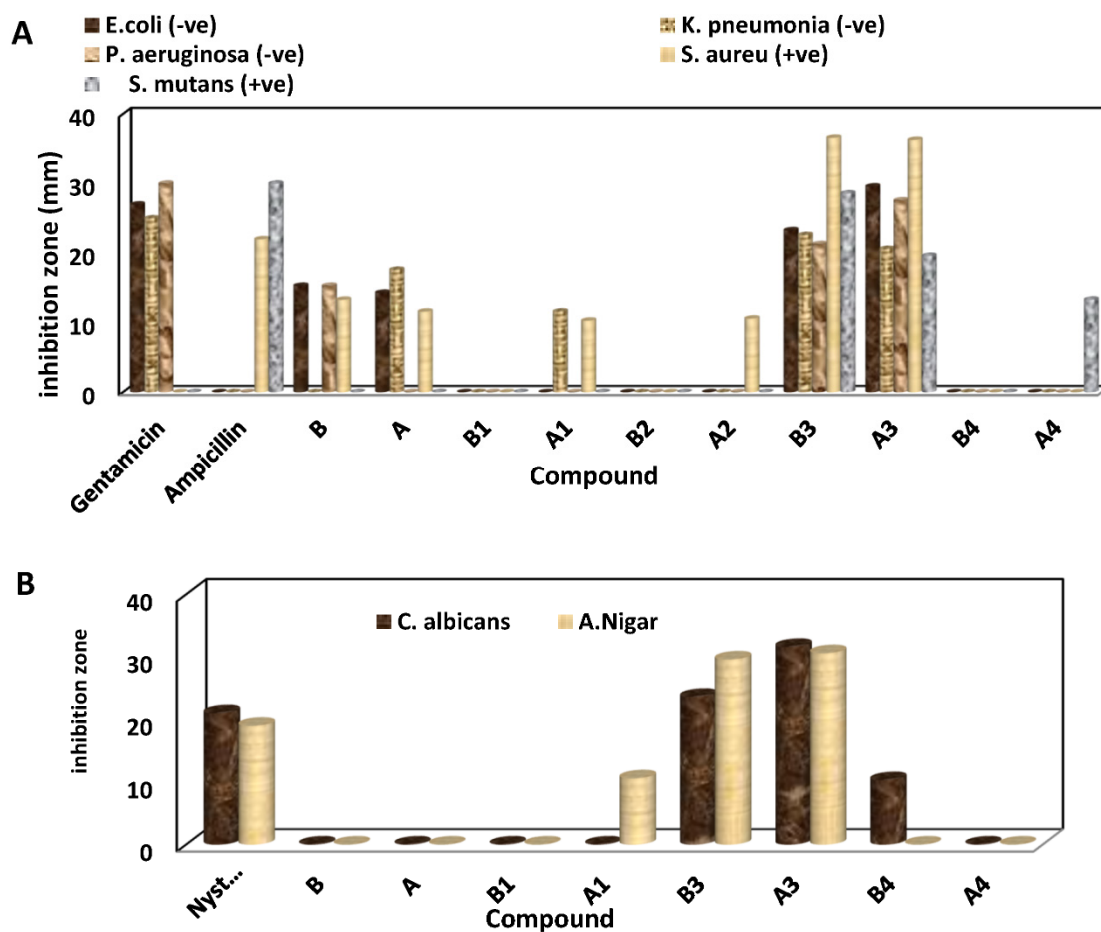


**Figure 7.** Graph showing the comparative (A) antibacterial activity of the ligand (A, B) and its complexes of Pb(II) (A<sub>1</sub>, B<sub>1</sub>), Mn(II), (A<sub>2</sub>, B<sub>2</sub>), Hg(II) (A<sub>3</sub>, B<sub>3</sub>), and Zn(II) (A<sub>4</sub>, B<sub>4</sub>) against gentamycin and ampicillin as the reference drugs; (B) antifungal bioassay of the same ligand and complexes against nystatin before (B, B<sub>1</sub>, B<sub>2</sub>, B<sub>3</sub>, and B<sub>4</sub>) and after irradiation (A, A<sub>1</sub>, A<sub>2</sub>, A<sub>3</sub>, and A<sub>4</sub>) at a concentration of 10 mg mL<sup>-1</sup> as the reference drug.

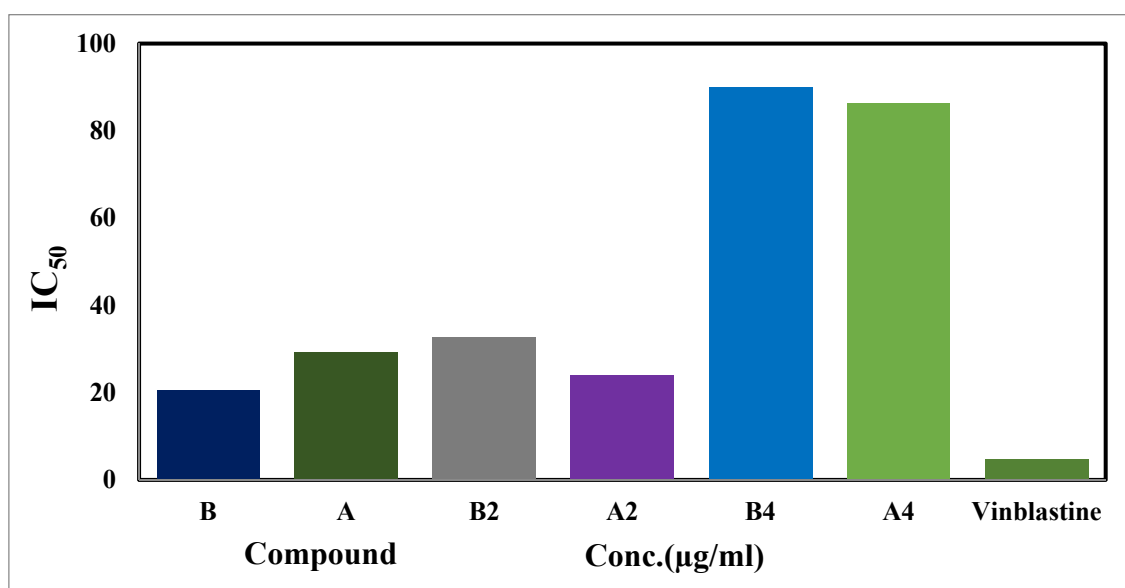


**Figure 8.** IC<sub>50</sub> values of the ligand (B, A) and Mn(II) (B<sub>2</sub>, A<sub>2</sub>) and Zn(II) (B<sub>4</sub>, A<sub>4</sub>) complexes before and after irradiation against the Hep-G2 carcinoma cell line compared to vinblastine.

**Table 9.** Cytotoxic activity (IC<sub>50</sub>) of the ligand and some metal complexes against human liver Hep-G2 and HEK-293 cell lines compared to vinblastine.

No	Compound	IC <sub>50</sub>	
		Hep-G2 Cell Line	HEK-293 Cell Line
B	H <sub>2</sub> L	20.45	90.10
A	H <sub>2</sub> L	29.25	91.40
B <sub>1</sub>	[Mn(H <sub>2</sub> L)(HL)]Cl	32.6	89.06
A <sub>1</sub>	[Mn(H <sub>2</sub> L)(HL)]Cl	23.95	88.50
B <sub>2</sub>	[Zn(H <sub>2</sub> L)(HL)]Cl	89.96	89.12
A <sub>2</sub>	[Zn(H <sub>2</sub> L)(HL)]Cl	86.24	89.01
Vinblastine		4.58	92.02

The attained IC<sub>50</sub> values of vinblastine, the ligand, and Mn(II) and Zn(II) complexes before and after irradiation are in the following order:

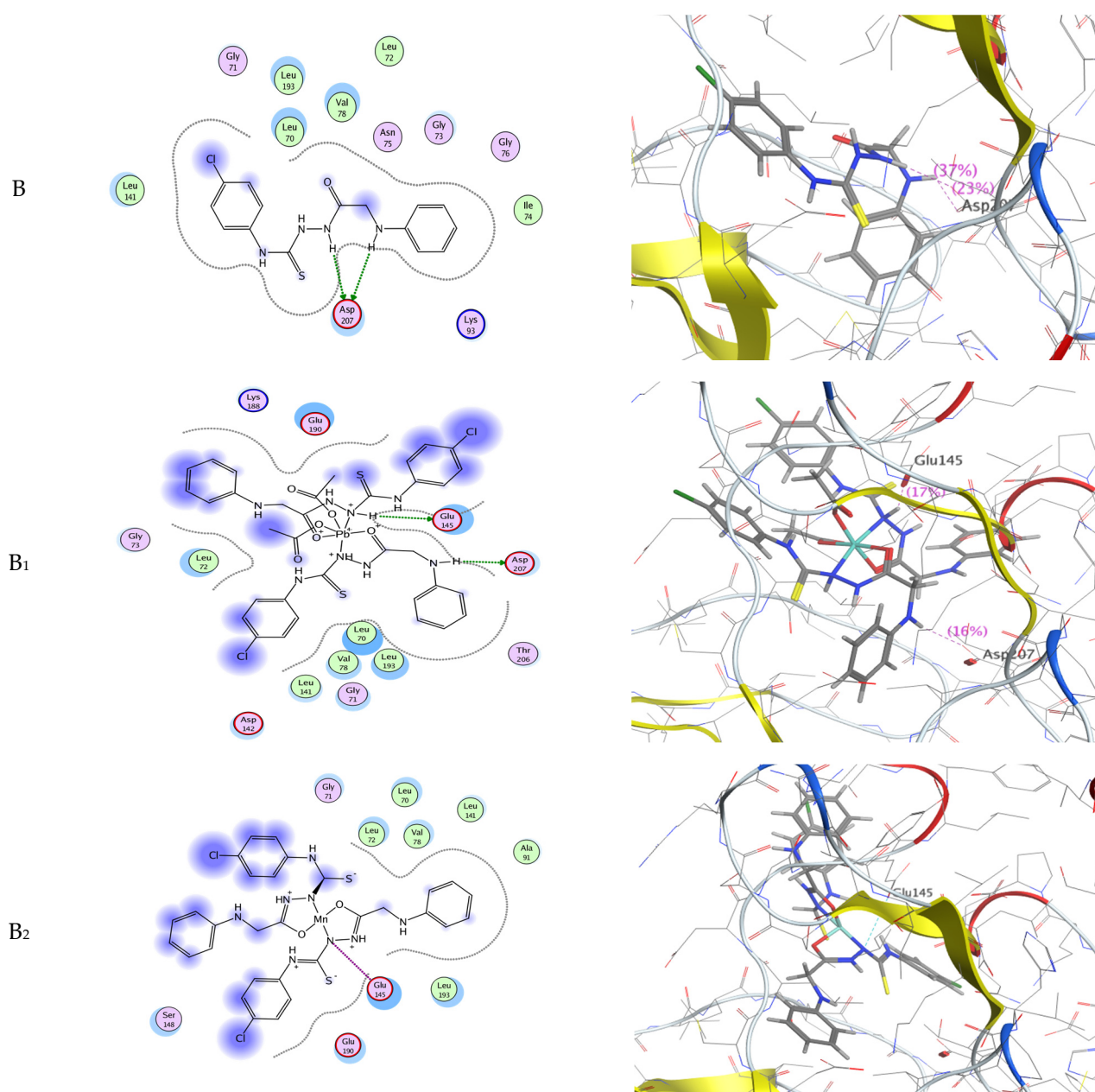
Vinblastine (4.58) > B (20.45) > A<sub>2</sub> (23.95) > A (29.45) > B<sub>2</sub>(32.6) > A<sub>4</sub> (86.24) > B<sub>4</sub> (189.96) µg/mL. These obtained results concluded that the synthesized ligand and its complexes have a good anticancer effect on the HepG2 cell line, except the Zn(II) complex before irradiation (B<sub>4</sub>) and Mn(II) complex after irradiation (A<sub>2</sub>), which are the most active ones. Moreover, vinblastine had an enhanced anticancer effect on the selected cancer cell lines.

### 3.8.3. Molecular Docking Studies

Various thiosemicarbazide derivatives have been used as starting materials for compounds with better biological activities. Molecular modeling tools are used to explore their mechanism of action. One of the most important enzymes that control signal transduction and cell proliferation is mitogen-activated protein kinase-activated protein kinase 2 (MAPKAPK-2 or MK-2) [44]. Discovering new inhibitors of this key enzyme has received attention as a strategy for discovering novel anticancer agents [45]. The ligand and its metal complexes were docked on the active site of the MK-2 enzyme in a trial to suggest a mechanism of action for their cytotoxicity. The protein data bank file is PDB: 3WI6). The file contains an MK-2 enzyme co-crystallized with an inhibitor. All docking procedures were achieved by MOE software. The inhibitor interacts with the MK-2 active site with Glu-145 hydrogen bonds involving Glu-145 and Asp 207 (Figure 9). The docking protocol was validated by redocking the Mn, Zn, and Pb complexes on the active site of the MK-2 enzyme with the highest energy score for the Pb complex (−7.28 kcal/mol). All the docked compounds were fitted on the active site of the MK-2 enzyme. The docking scores and amino acid interactions for the docked compounds are summarized in Table 10. The types of interactions involved were side-chain acceptor, metal contact receptor, and solvent contact. The Hg compound displayed the best docking score (−8.16 kcal/mol), which may explain its promising cytotoxic activity. Finally, we can conclude that the molecular docking of our compounds on the active site of the mitogen-activated kinase (MK-2) revealed good amino acid interactions. We observed good agreement between the experimental IC<sub>50</sub> values and the molecular docking of the selected enzyme target relative to the Pb and Mn complexes, but the ligand scoring energy sequence was not compatible with its IC<sub>50</sub> value.

**Table 10.** Comparison of binding affinity of the complexes against the active pocket of mitogen-activated kinase (MK-2) (PDB ID: 3WI6).

Compound	Involved Amino Acids (Scoring Energy kcal/mol)	Type of Interaction
H <sub>2</sub> L	Asp-207 (−3.14)	Side chain acceptor
[Pb(H <sub>2</sub> L) <sub>2</sub> (OAc) <sub>2</sub> ]EtOH.H <sub>2</sub> O	Glu-145 and Asp-207 (−7.28)	Side chain acceptor
[Mn(H <sub>2</sub> L)(HL)]Cl	Glu-145 (−5.55)	Metal contact receptor
[Hg <sub>2</sub> (H <sub>2</sub> L)(OH)SO <sub>4</sub> ]	(−8.16)	Solvent contact
[Zn(H <sub>2</sub> L)(HL)]Cl	Glu-145 (−5.79)	Metal contact receptor

**Figure 9.** Cont.

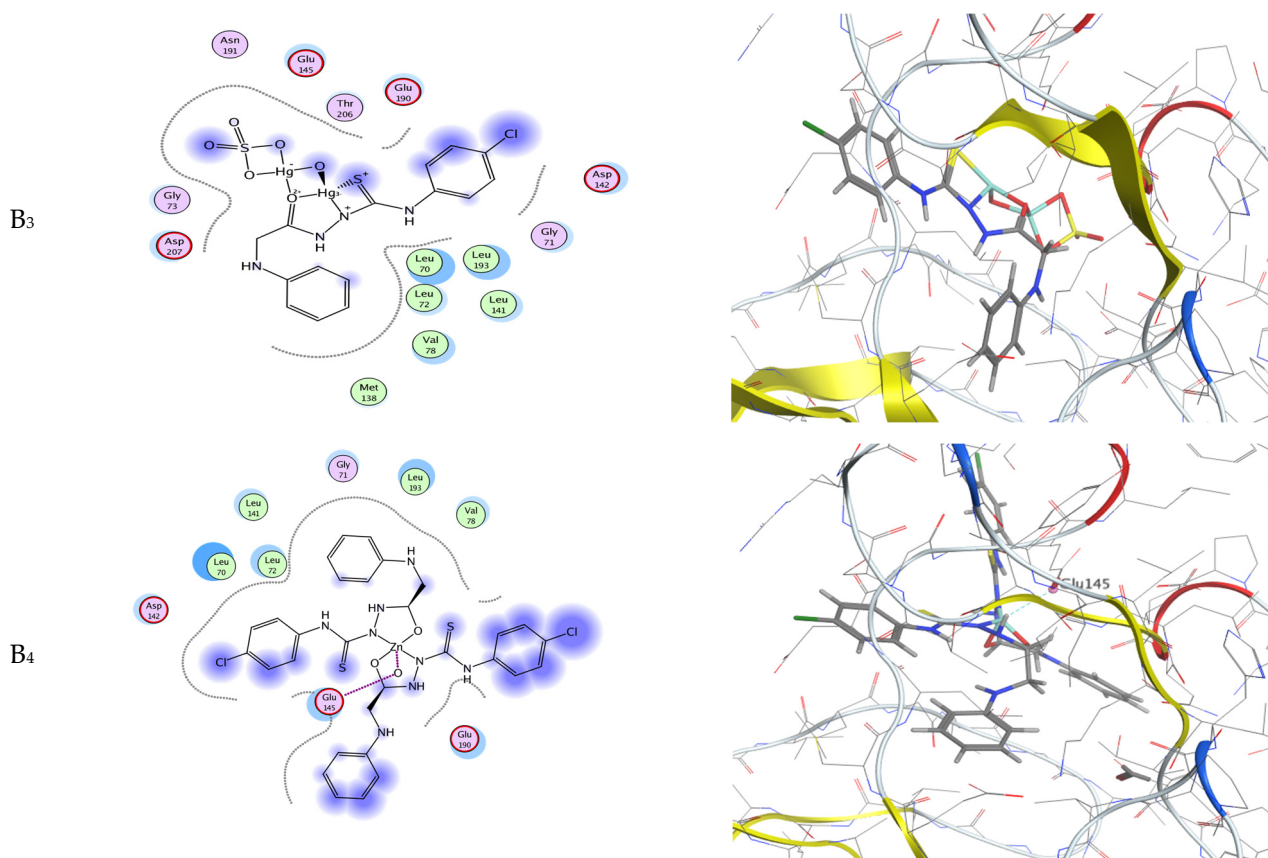


**Figure 9.** Binding pose of ligand (B) and the Pb(II), Mn(II), Hg(II), and Zn(II) complexes in the active pocket of mitogen-activated kinase (MK-2) (PDB ID: 3WI6).

#### 4. Conclusions

New Pb(II), Mn(II), Hg(II), and Zn(II) complexes were prepared, and their molecular structures were described before and after  $\gamma$ -irradiation. The results documented the following:

- 1 The ligand behaves as a monobasic or neutral tetradentate in complexes B<sub>1</sub>, B<sub>2</sub>, and B<sub>4</sub>, while complex (B<sub>3</sub>) is binuclear.
- 2 The DFT study showed the suggested geometrical structures of our compounds.
- 3 Based on the results obtained from the FT-IR spectra of complexes before (B<sub>1</sub>–B<sub>4</sub>) and after (A<sub>1</sub>–A<sub>4</sub>) irradiation, the band of spectra after irradiation was sharper than before.
- 4 No significant change was detected in the structures, and only a slight shift in the wavelength and the absorbance after the exposure to gamma-ray.
- 5 According to the powder X-ray results, it was noticed that the calculated crystalline size of the ligand and complexes fell within the nano range.
- 6 Mn(II) complex after irradiation against the human liver cancer cell line (HepG2) reflected higher anti-cancer activity than the ligand and Zn(II) complexes.
- 7 The molecular docking showed that all the compounds have a potential antitumor effect, especially the Hg chelate with a more negative scoring energy value, which is expected to inhibit the active site of mitogen activated kinase (MK-2).

**Supplementary Materials:** The following are available online, Figure S1a: FT-IR spectra of Mn(II) complexes before (B2) and after (A2) irradiation; Figure S1b: FT-IR of spectra of Hg(II) complexes before (B3) and after (A3) irradiation; Figure S1c: FT-IR of spectra of Zn(II) complexes before (B4) and after (A4) irradiation; Figure S2: PXRD powder pattern of of Zn(II) complex before (B4) and after irradiation (A4); Figure S3: Optimized 3D structures of ligand (B) and the Pb(II) B1, Mn(II) B2, Hg(II) B3, and Zn(II) B4 complexes; Figure S4: IC50 Values of Ligand (B, A) and Mn(II) (B2, A2)

and Zn(II) (B4, A4) complexes before and after irradiation against HEK-293 cell line compared to Vinblastine; Tables S1–S5: The coordinates of the optimized ligand (B) and their metal complexes; Table S6: Antimicrobial activity of unirradiated and irradiated complexes.

**Author Contributions:** Conceptualization, E.M.A. and S.A.A.; methodology, E.M.A., S.A.A. and H.A.; software, S.S.H.; validation, E.M.A. and S.A.A.; formal analysis, E.M.A. and S.A.A.; investigation, E.M.A. and H.A.; resources, H.H.E. and H.A.; data curation, E.M.A. and H.H.E.; writing—original draft preparation, E.M.A.; writing—review and editing, E.M.A. and S.A.A.; visualization, S.A.A., E.M.A. and H.A.; supervision, S.A.A. All authors have read and agreed to the published version of the manuscript.

**Funding:** This research received no external funding.

**Institutional Review Board Statement:** Not applicable.

**Informed Consent Statement:** Not applicable.

**Data Availability Statement:** The data presented in this study are available on request from the corresponding author.

**Conflicts of Interest:** The authors declare no conflict of interest.

## References

1. Chen, J.; Huang, Y.-W.; Liu, G.; Afrasiabi, Z.; Sinn, E.; Padhye, S.; Ma, Y. The Cytotoxicity and Mechanisms of 1, 2-Naphthoquinone Thiosemicarbazone and its Metal Derivatives Against MCF-7 Human Breast Cancer Cells. *Toxicol. Appl. Pharmacol.* **2004**, *197*, 40–48. [[CrossRef](#)] [[PubMed](#)]
2. Murphy, M.B.; Mercer, S.L.; Dewese, J.E. Inhibitors and Poisons of Mammalian Type Ii Topoisomerases. In *Advances In Molecular Toxicology*; Elsevier: Amsterdam, The Netherlands, 2017; Volume 11, pp. 203–240.
3. Ateş, D.; Gulcan, M.; Gümüş, S.; Şekerci, M.; Özdemir, S.; Şahin, E.; Çolak, N. Synthesis of Bis (Thiosemicarbazone) Derivatives: Definition, Crystal Structure, Biological Potential and Computational Analysis. *Phosphorus Sulfur Relat. Elem.* **2018**, *193*, 14–22. [[CrossRef](#)]
4. Ramachandran, R.; Rani, M.; Kabilan, S. Design, Synthesis and Biological Evaluation of Novel 2-[(2, 4-Diaryl-3-Azabicyclo [3.3. 1] Nonan-9-Ylidene) Hydrazono]-1, 3-Thiazolidin-4-Ones as a New Class of Antimicrobial Agents. *Bioorg. Med. Chem. Lett.* **2009**, *19*, 2819–2823. [[CrossRef](#)] [[PubMed](#)]
5. Kovala-Demertzi, D.; Miller, J.R.; Kourkoumelis, N.; Hadjikakou, S.K.; Demertzis, M.A. Palladium (Ii) and Platinum (Ii) Complexes of Pyridine-2-Carbaldehyde Thiosemicarbazone with Potential Biological Activity. Synthesis, Structure and Spectral Properties. Extended Network via Hydrogen Bond Linkages of [Pd (Pyts) Cl]. *Polyhedron* **1999**, *18*, 1005–1013. [[CrossRef](#)]
6. Finch, R.A.; Liu, M.-C.; Grill, S.P.; Rose, W.C.; Loomis, R.; Vasquez, K.M.; Cheng, Y.-C.; Sartorelli, A.C. Triapine (3-Aminopyridine-2-Carboxaldehyde-Thiosemicarbazone): A Potent Inhibitor of Ribonucleotide Reductase Activity with Broad Spectrum Antitumor Activity. *Biochem. Pharmacol.* **2000**, *59*, 983–991. [[CrossRef](#)]
7. Sharma, S.; Athar, F.; Maurya, M.R.; Azam, A. Copper (Ii) Complexes with Substituted Thiosemicarbazones of Thiophene-2-Carboxaldehyde: Synthesis, Characterization and Antiamoebic Activity Against *E. Histolytica*. *Eur. J. Med. Chem.* **2005**, *40*, 1414–1419. [[CrossRef](#)] [[PubMed](#)]
8. Parrilha, G.L.; Da Silva, J.G.; Gouveia, L.F.; Gasparoto, A.K.; Dias, R.P.; Rocha, W.R.; Santos, D.A.; Speziali, N.L.; Beraldo, H. Pyridine-Derived Thiosemicarbazones and Their Tin (Iv) Complexes with Antifungal Activity against *Candida* Spp. *Eur. J. Med. Chem.* **2011**, *46*, 1473–1482. [[CrossRef](#)]
9. Alomar, K.; Gaumet, V.; Allain, M.; Bouet, G.; Landreau, A. Synthesis, Crystal Structure, Characterisation, and Antifungal Activity of 3-Thiophene Aldehyde Semicarbazone (3stch), 2, 3-Thiophene Dicarboxaldehyde Bis (Semicarbazone) (2, 3bstch2) and Their Nickel (Ii) Complexes. *J. Inorg. Biochem.* **2012**, *115*, 36–43. [[CrossRef](#)]
10. Usman, A.; Razak, I.A.; Chantrapromma, S.; Fun, H.-K.; Sreekanth, A.; Sivakumar, S.; Prathapachandra Kurup, M. Bis [1-(Pyridin-2-Yl) Ethanone-Kn 4-Phenylthiosemicarbazono-K2n4, S] Manganese (Ii). *Acta Crystallogr., Sect. C: Cryst. Struct. Commun.* **2002**, *58*, M461–M463. [[CrossRef](#)]
11. Kaya, B.; Yılmaz, Z.K.; Şahin, O.; Aslim, B.; Tükenmez, Ü.; Ülküseven, B. Structural Analysis and Biological Functionalities of Iron (Iii)-and Manganese (Iii)-Thiosemicarbazone Complexes: In Vitro Anti-Proliferative Activity on Human Cancer Cells, Dna Binding and Cleavage Studies. *J. Biol. Inorg. Chem.* **2019**, *24*, 365–376. [[CrossRef](#)]
12. Kumar, L.V.; Nath, G.R. Synthesis, Characterization and Biological Studies of Cobalt (Ii), Nickel (Ii), Copper (Ii) and Zinc (Ii) Complexes of Vanillin-4-Methyl-4-Phenyl-3-Thiosemicarbazone. *J. Chem. Sci.* **2019**, *131*, 1–13. [[CrossRef](#)]
13. El-Boraey, H.A.; Mansour, A.I. Synthesis, Spectral and Gamma Ray Irradiation Studies on Metal Complexes of N, N'-Naphthalene-1, 8-Diylbis (2-Aminobenzamide). *Inorg. Nano-Met. Chem.* **2018**, *48*, 8–15. [[CrossRef](#)]
14. El-Boraey, H.; El-Gammal, O.; Sattar, N.A. Impact of Gamma-Ray Irradiation on Some Aryl-Amide-Bridged Schiff-Base Complexes: Spectral, Tga, Xrd, and Antioxidant Properties. *J. Radioanal. Nucl. Chem.* **2020**, *323*, 241–252. [[CrossRef](#)]

15. Marzouk, M.; Elbatal, F.; Abdelghany, A. Ultraviolet and Infrared Absorption Spectra of Cr<sub>2</sub>O<sub>3</sub> Doped–Sodium Metaphosphate, Lead Metaphosphate and Zinc Metaphosphate Glasses and Effects of Gamma Irradiation: A Comparative Study. *Spectrochim. Acta A Mol. Biomol. Spectrosc.* **2013**, *114*, 658–667. [[CrossRef](#)] [[PubMed](#)]
16. Neacsu, A.; Gheorghe, D.; Marinescu, C.; Stancu, E.; Tecuceanu, V.; Ciuculescu, C. The Effect of Gamma Rays Upon L-Proline and 4-Hydroxy-L-Proline. A Thermochemical Study. *Radiat. Phys. Chem.* **2019**, *156*, 115–127. [[CrossRef](#)]
17. Aly, S.; El-Boraey, H.A. Effect of Gamma Irradiation on Spectral, Xrd, Sem, Dna Binding, Molecular Modling and Antibacterial Property of Some (Z) N-(Furan-2-Yl) Methylene)-2-(Phenylamino) Acetohydrazide Metal (Ii) Complexes. *J. Mol. Struct* **2019**, *1185*, 323–332. [[CrossRef](#)]
18. Aly, S.A.; Eldourghamy, A.S. Synthesis, Characterization of New Copper Complexes of Thiosemicarbazone Derivatives and Their Biological Activities. *Int. J. Res. Chem. Environ.* **2017**, *7*, 38–46.
19. Basset, J.; Denney, R.; Jeffery, G.; Mendham, J. Vogel's Textbook of Quantitative Inorganic Analysis. *Longman Group Ltd.* **1978**, 319.
20. Nair, M.; Appukuttan, A.S. Syntheses, Spectral, Surface Morphological and Gamma Ray Irradiation Studies of Some Oxomolybdenum (V) and Dioxomolybdenum (Vi) Complexes of an Azo Dye Derived from 4-Aminoantipyrine. *J. Korean Chem. Soc.* **2012**, *56*, 217–227. [[CrossRef](#)]
21. Hassan, S.S. Antibacterial, Dft and Molecular Docking Studies of Rh (Iii) Complexes of Coumarinyl-Thiosemicarbazone Nuclei Based Ligands. *Appl. Organomet. Chem.* **2018**, *32*, E4170. [[CrossRef](#)]
22. Hassan, S.S.; Gomha, S.M. Novel Functionalized Thiosemicarbazone Ligands and Their Pd (Ii) Complexes: Synthesis, Characterization, Antibacterial and Cytotoxic Activities. *Chem. Pap.* **2019**, *73*, 331–344. [[CrossRef](#)]
23. Sapundzhi, F.; Dzimbova, T. Computer Modelling of The Cb1 Receptor by Molecular Operating Environment. *Bulg. Chem. Commun.* **2018**, *50*, 15–19.
24. Aly, S.A.; Elganzory, H.H.; Mahross, M.H.; Abdalla, E.M. Quantum Chemical Studies and Effect of Gamma Irradiation on the Spectral, Thermal, X-Ray Diffraction and Dna Interaction with Pd (Ii), Cu (I), and Cd (Ii) of Hydrazone Derivatives. *Appl. Organomet. Chem.* **2021**, *35*, E6153. [[CrossRef](#)]
25. Balouiri, M.; Sadiki, M.; Ibnsouda, S.K. Methods for in vitro Evaluating Antimicrobial Activity: A Review. *J. Pharm. Anal.* **2016**, *6*, 71–79. [[CrossRef](#)]
26. Melloul, E.; Roisin, L.; Durieux, M.-F.; Woerther, P.-L.; Jenot, D.; Risco, V.; Guillot, J.; Dannaoui, E.; Decousser, J.-W.; Botterel, F. Interactions of *Aspergillus Fumigatus* and *Stenotrophomonas Maltophilia* in an in vitro Mixed Biofilm Model: Does The Strain Matter? *Front. Microbiol.* **2018**, *9*, 2850. [[CrossRef](#)]
27. Abdalla, E.M.; Abdel Rahman, L.H.; Abdelhamid, A.A.; Shehata, M.R.; Alothman, A.A.; Nafady, A. Synthesis, Characterization, Theoretical Studies, And Antimicrobial/Antitumor Potencies of Salen and Salen/Imidazole Complexes of Co (Ii), Ni (Ii), Cu (Ii), Cd (Ii), Al (Iii) and La (Iii). *Appl. Organomet. Chem.* **2020**, *34*, E5912. [[CrossRef](#)]
28. Al-Farhan, B.S.; Basha, M.T.; Abdel Rahman, L.H.; El-Saghier, A.M.; El-Ezz, A.; Marzouk, A.A.; Shehata, M.R.; Abdalla, E.M. Synthesis, Dft Calculations, Antiproliferative, Bactericidal Activity and Molecular Docking of Novel Mixed-Ligand Salen/8-Hydroxyquinoline Metal Complexes. *Molecules* **2021**, *26*, 4725. [[CrossRef](#)]
29. Geary, W.J. The Use of Conductivity Measurements in Organic Solvents for the Characterisation of Coordination Compounds. *Coord. Chem. Rev.* **1971**, *7*, 81–122. [[CrossRef](#)]
30. Abou Sekkina, M.M.; Kashar, T.I.; Aly, S.A. Spectrochemical Study and Effect of High Energatic Gamma Ray on Copper (Ii) Complexes. *Solid State Sci.* **2011**, *13*, 2080–2085. [[CrossRef](#)]
31. Shankarwar, S.G.; Nagolkar, B.B.; Shelke, V.A.; Chondhekar, T.K. Synthesis, Spectral, Thermal and Antimicrobial Studies of Transition Metal Complexes of 14-Membered Tetraaza [N<sub>4</sub>] Macrocyclic Ligand. *Spectrochim. Acta A Mol. Biomol. Spectrosc.* **2015**, *145*, 188–193. [[CrossRef](#)]
32. El-Boraey, H.A.; El-Gammal, O.A. New 15-Membered Tetraaza (N<sub>4</sub>) Macrocyclic Ligand and its Transition Metal Complexes: Spectral, Magnetic, Thermal and Anticancer Activity. *Spectrochim. Acta A Mol. Biomol. Spectrosc.* **2015**, *138*, 553–562. [[CrossRef](#)]
33. Sabounchei, S.J.; Bagherjeri, F.A.; Boskovic, C.; Gable, R.W.; Karamian, R.; Asadbegy, M. Binuclear Mercury (Ii) Complexes of Sulfonium Ylides: Synthesis, Structural Characterization and Anti-Bacterial Activity. *J. Mol. Struct* **2013**, *1034*, 265–270. [[CrossRef](#)]
34. Sabounchei, S.J.; Sedghi, A.; Bayat, M.; Hosseinzadeh, M.; Hashemi, A.; Yousefi, A.; Gable, R.W. Binuclear Mercury (Ii) Complexes of Ambidentate Sulfonium Ylides in Comparison with Analogous Phosphonium-Based Complexes; Synthesis, Characterization and a Comprehensive Theoretical Study. *J. Mol. Struct* **2019**, *1175*, 346–356. [[CrossRef](#)]
35. El-Metwaly, N.M.; Refat, M.S. Elaborated 1h Nmr Study for the Ligitational Behavior of Two Thiosemicarbazide Derivatives towards Some Heavy Metals (Sn (Ii), Sb (Iii), Pb (Ii) And Bi (Iii)), Thermal, Antibacterial and Antifungal Studies. *Spectrochim. Acta A Mol. Biomol. Spectrosc.* **2011**, *81*, 519–528. [[CrossRef](#)]
36. Abu-Khadra, A.S.; Farag, R.S.; Abdel-Hady, A.E.-D.M. Synthesis, Characterization and Antimicrobial Activity of Schiff Base (E)-N-(4-(2-Hydroxybenzylideneamino) Phenylsulfonyl) Acetamide Metal Complexes. *Am. J. Anal. Chem.* **2016**, *7*, 233. [[CrossRef](#)]
37. Hassan, S.S.; Mohamed, E.F. Antimicrobial, Antioxidant and Antitumor Activities of Nano-Structure Eu (Iii) and La (Iii) Complexes with Nitrogen Donor Tridentate Ligands. *Appl. Organomet. Chem.* **2020**, *34*, E5258. [[CrossRef](#)]
38. Chandra, S.; Gautam, S.; Rajor, H.K.; Bhatia, R. Syntheses, Spectroscopic Characterization, Thermal Study, Molecular Modeling, and Biological Evaluation of Novel Schiff's Base Benzil Bis (5-Amino-1, 3, 4-Thiadiazole-2-Thiol) with Ni (Ii), and Cu (Ii) Metal Complexes. *Spectrochim. Acta A Mol. Biomol. Spectrosc.* **2015**, *137*, 749–760. [[CrossRef](#)]

39. El-Gammal, O.A.; Alshater, H.; El-Boraey, H.A. Schiff Base Metal Complexes of 4-Methyl-1h-Indol-3-Carbaldehyde Derivative as a Series of Potential Antioxidants and Antimicrobial: Synthesis, Spectroscopic Characterization and 3D Molecular Modeling. *J. Mol. Struct* **2019**, *1195*, 220–230. [[CrossRef](#)]
40. Belaid, S.; Landreau, A.; Djebbar, S.; Benali-Baitich, O.; Bouet, G.; Bouchara, J.-P. Synthesis, Characterization and Antifungal Activity of a Series of Manganese (Ii) and Copper (Ii) Complexes with Ligands Derived from Reduced N, N'-O-Phenylenebis (Salicylideneimine). *J. Inorg. Biochem.* **2008**, *102*, 63–69. [[CrossRef](#)]
41. Ejidike, I.P. Cu (Ii) Complexes of 4-[(1e)-N-{2-[(Z)-Benzylidene-Amino] Ethyl} Ethanimidoyl] Benzene-1, 3-Diol Schiff Base: Synthesis, Spectroscopic, in-vitro Antioxidant, Antifungal and Antibacterial Studies. *Molecules* **2018**, *23*, 1581. [[CrossRef](#)]
42. Abdel-Rahman, L.H.; Ismail, N.M.; Ismael, M.; Abu-Dief, A.M.; Ahmed, E.A.-H. Synthesis, Characterization, Dft Calculations and Biological Studies of Mn (Ii), Fe (Ii), Co (Ii) and Cd (Ii) Complexes Based on a Tetradentate Onno Donor Schiff Base Ligand. *J. Mol. Struct* **2017**, *1134*, 851–862. [[CrossRef](#)]
43. El-Boraey, H.A.; El-Salamony, M.A. Transition Metal Complexes with Polydentate Ligand: Synthesis, Characterization, 3D Molecular Modelling, Anticancer, Antioxidant and Antibacterial Evaluation. *J. Inorg. Organomet. Polym. Mater.* **2019**, *29*, 684–700. [[CrossRef](#)]
44. Kotlyarov, A.; Neininger, A.; Schubert, C.; Eckert, R.; Birchmeier, C.; Volk, H.-D.; Gaestel, M. Mapkap Kinase 2 is Essential for Lps-Induced Tnf-A Biosynthesis. *Nat. Cell Biol.* **1999**, *1*, 94–97. [[CrossRef](#)] [[PubMed](#)]
45. Haddad, J.J. Vx-745 (Vertex Pharmaceuticals). *Curr. Opin. Investig. Drugs* **2001**, *2*, 1070–1076. [[PubMed](#)]